

The clustering of galaxies in the SDSS-III Baryon Oscillation Spectroscopic Survey: testing gravity with redshift space distortions using the power spectrum multipoles

Florian Beutler,^{1★} Shun Saito,^{1,2,3,4} Hee-Jong Seo,^{5,6} Jon Brinkmann,⁷
 Kyle S. Dawson,⁸ Daniel J. Eisenstein,⁹ Andreu Font-Ribera,¹ Shirley Ho,^{10,11}
 Cameron K. McBride,⁹ Francesco Montesano,¹² Will J. Percival,¹³ Ashley J. Ross,¹³
 Nicholas P. Ross,^{1,14} Lado Samushia,¹³ David J. Schlegel,¹ Ariel G. Sánchez,¹²
 Jeremy L. Tinker¹⁵ and Benjamin A. Weaver¹⁵

Affiliations are listed at the end of the paper

Accepted 2014 May 27. Received 2014 May 27; in original form 2013 December 4

ABSTRACT

We analyse the anisotropic clustering of the Baryon Oscillation Spectroscopic Survey (BOSS) CMASS Data Release 11 (DR11) sample, which consists of 690 827 galaxies in the redshift range $0.43 < z < 0.7$ and has a sky coverage of 8498 deg^2 . We perform our analysis in Fourier space using a power spectrum estimator suggested by Yamamoto et al. We measure the multipole power spectra in a self-consistent manner for the first time in the sense that we provide a proper way to treat the survey window function and the integral constraint, without the commonly used assumption of an isotropic power spectrum and without the need to split the survey into subregions. The main cosmological signals exploited in our analysis are the baryon acoustic oscillations and the signal of redshift space distortions, both of which are distorted by the Alcock–Paczynski effect. Together, these signals allow us to constrain the distance ratio $D_V(z_{\text{eff}})/r_s(z_d) = 13.89 \pm 0.18$, the Alcock–Paczynski parameter $F_{\text{AP}}(z_{\text{eff}}) = 0.679 \pm 0.031$ and the growth rate of structure $f(z_{\text{eff}})\sigma_8(z_{\text{eff}}) = 0.419 \pm 0.044$ at the effective redshift $z_{\text{eff}} = 0.57$. We emphasize that our constraints are robust against possible systematic uncertainties. In order to ensure this, we perform a detailed systematics study against CMASS mock galaxy catalogues and N -body simulations. We find that such systematics will lead to 3.1 per cent uncertainty for $f\sigma_8$ if we limit our fitting range to $k = 0.01\text{--}0.20 \text{ h Mpc}^{-1}$, where the statistical uncertainty is expected to be three times larger. We did not find significant systematic uncertainties for D_V/r_s or F_{AP} . Combining our data set with Planck to test General Relativity (GR) through the simple γ -parametrization, where the growth rate is given by $f(z) = \Omega_m^\gamma(z)$, reveals a $\sim 2\sigma$ tension between the data and the prediction by GR. The tension between our result and GR can be traced back to a tension in the clustering amplitude σ_8 between CMASS and Planck.

Key words: gravitation – surveys – cosmological parameters – cosmology: observations – dark energy – large-scale structure of Universe.

1 INTRODUCTION

The key to understand the dynamical properties of the Universe, its past and its future, is the understanding of gravity. Today’s dominant theory of the origin of the Universe, the big bang model, is based on

Albert Einstein’s General Relativity (GR). The crucial idea behind GR, the connection between space and time into space–time first allowed us to talk about curved space and expanding space, terms which do not exist in Newton’s gravity.

GR is a very powerful theory, which makes many testable predictions, like the deflection of light or gravitational waves. Despite the successes of our current understanding of gravity, there are several problems, which motivated scientists to search for alternative

★E-mail: fbeutler@lbl.gov

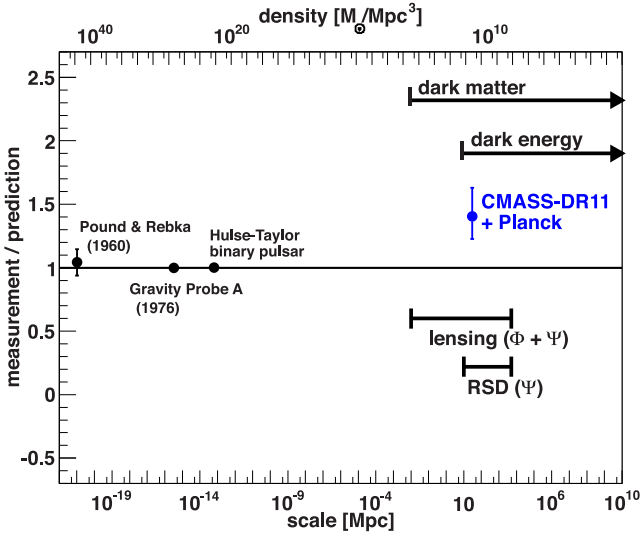


Figure 1. Summary of different tests of GR as a function of distance scale (bottom axis) and densities (top axis). The standard model of cosmology seems to run into problems (dark matter and dark energy) at large scales. Because these problems could indicate a breakdown of GR we need to test GR on large scales. Two probes which can do this are RSD and lensing. While RSD measures the Newtonian potential Ψ , lensing measures the sum of the metric potentials $\Phi + \Psi$. However, any modification of gravity needs to pass the very precise tests on smaller scales (Pound and Rebka experiment; Pound & Rebka 1960, Gravity Probe A; Vessot et al. 1980, Hulse–Taylor binary pulsar; Hulse & Taylor 1975, see Will 2006 for a complete list). Note that the error bars for Gravity Probe A and the Hulse–Taylor binary pulsar are smaller than the data points in this plot. In this analysis, we perform a Λ CDM consistency test (blue data point), where we use the CMASS-DR11 power spectrum multipoles together with Planck (Ade et al. 2013a) to test GR on scales of ~ 30 Mpc (see Section 9.1).

formulations or expansions of GR. One problem, which we will not pursue any further in this paper, is that GR cannot be combined with the other fundamental forces, since GR is not formulated as a quantum field theory. Another problem is that the motions of galaxies and galaxy clusters cannot be explained by GR and baryonic matter alone, but require the introduction of a new form of matter, so-called dark matter (Zwicky 1937; Kahn & Woltjer 1959; Freeman 1970; Rubin & Ford 1970), which nobody has yet observed directly. While the issue of dark matter has existed since the 1930s, in the late 1990s Type Ia supernova surveys made the intriguing discovery that the expansion of the Universe is accelerating (Riess et al. 1998; Perlmutter et al. 1999). This required the introduction of yet another dark component, so-called dark energy, which would counteract the gravitational force leading to an accelerated expansion. The question now is whether these problems indicate a breakdown of GR or whether there are additional unknown components of the Universe. While the problems of GR on cosmological scales (dark matter and dark energy) gave birth to many new models of gravity (see e.g. Jain & Khoury 2010; Clifton et al. 2012; Capozziello & Laurentis 2013), so far none of these models has been able to convince scientists that it is time to abandon GR.

Given that it is on cosmological scales where GR runs into trouble, it is on cosmological scales where we have to test GR. Fig. 1 shows different tests of GR at different scales (see e.g. Will 2006). One interesting observable, which allows us to test GR on cosmic scales, is redshift space distortions (RSD; Sargent & Turner 1977; Kaiser 1987; Hamilton 1998). RSD are peculiar velocities of galaxies due to gravitational interaction. The line-of-sight component of

this additional velocity cannot be easily separated from the Hubble flow, and contaminates our measurement of the cosmic expansion. This makes the observed galaxy clustering anisotropically distorted, since the line-of-sight direction becomes ‘special’. This is what we call RSD. The anisotropic pattern of RSDs in galaxy clustering allows us to extract information on the peculiar velocities which are directly related to the Newton potential through the Euler equation. Given the amount of matter in the Universe, GR makes a clear and testable prediction for the amplitude of this anisotropic signal. In the last decade, galaxy redshift surveys became large enough to test this prediction (Peacock et al. 2001; Hawkins et al. 2003; Tegmark et al. 2006; Guzzo et al. 2008; Yamamoto, Sato & Huetsi 2008; Blake et al. 2011a; Beutler et al. 2012; Reid et al. 2012; Chuang et al. 2013a; Nishimichi & Oka 2013; Samushia et al. 2013a).

In addition to the RSD signal, the galaxy power spectrum and correlation function carry geometric information. The measurement of the baryon acoustic oscillation (BAO) scale in the distribution of galaxies has become one of the most powerful probes of cosmology, together with the cosmic microwave background (CMB; Ade et al. 2013a). The BAO scale has now been detected at several different redshifts (Eisenstein et al. 2005; Beutler et al. 2011; Blake et al. 2011b; Anderson et al. 2012, 2013b; Padmanabhan et al. 2012; Slosar et al. 2013). Most notably the ongoing Baryon Oscillation Spectroscopic Survey (BOSS) (Schlegel et al. 2009) reduced the measurement uncertainty on the BAO scale to 1 per cent (Anderson et al. 2013b), which is still considerably larger than the expected systematic bias (Eisenstein & White 2004; Padmanabhan & White 2009; Mehta et al. 2011). Measuring the galaxy clustering along the line of sight and perpendicular to the line of sight allows us to perform an Alcock–Paczynski (AP) test (Alcock & Paczynski 1979; Ballinger, Peacock & Heavens 1996; Matsubara & Suto 1996) with both the RSD and BAO signals. The AP test describes a distortion in an otherwise isotropic feature in the galaxy clustering when the assumed fiducial cosmological model used to transfer the measured redshifts into distances deviates from the true cosmology. This anisotropic signal may appear degenerate with the RSD signal in a featureless power spectrum. Using the BAO signal, we can break this degeneracy and exploit all three signals, RSD, BAO and the AP effect for cosmological parameter constraints.

In this analysis, we are going to use the CMASS sample of BOSS galaxies that will be included in the Sloan Digital Sky Survey (SDSS) Data Release 11 (DR11), which will become publicly available together with the final data (DR12) at the end of 2014. We use this data set to constrain the growth of structure and the geometry of the Universe simultaneously. We measure the growth rate via the parameter combination $f(z)\sigma_8(z)$ and the geometry of the Universe via $D_V(z)/r_s(z_d)$ and $F_{AP}(z) = (1+z)D_A(z)H(z)/c$ at an effective redshift of $z_{\text{eff}} = 0.57$. The BAO signal and the AP effect constrain the geometry, i.e. $D_V(z)/r_s(z_d)$ and $F_{AP}(z)$, thereby isolating the anisotropy in the clustering amplitude due to the RSD. The growth rate, $f(z)\sigma_8(z)$, is constrained by this RSD signal. We will make our analysis in Fourier space using the power spectrum monopole and quadrupole. The power spectrum multipoles are measured using a new power spectrum estimator suggested by Yamamoto et al. (2006). The popular power spectrum estimator suggested by Feldman, Kaiser & Peacock (1994) (from here on FKP estimator) cannot be used to make angle-dependent measurements in BOSS because of the plane-parallel approximation that this estimator implicitly makes (see Section 3 for details).

Since the power spectrum quadrupole is more sensitive to window function effects than the more commonly used monopole, we suggest a new way of including the window function into the power

spectrum analysis. In order to robustly constrain the RSD and AP-test parameters, we model the anisotropic galaxy power spectrum using perturbation theory (PT) which fairly reflects a series of recent theoretical progresses. Our PT model accurately describes non-linear issues such as gravitational evolution, mapping from real to redshift space, and local and non-local galaxy bias. We also perform a detailed study of possible systematic uncertainties and quantify a systematic error for our parameter constraints. Our analysis has been done ‘blind’, meaning that all model tests and the set-up of the fitting conditions are investigated using mock data and only at the final stage do we fit the actual CMASS-DR11 measurements. The CMASS-DR11 constraints on $D_V(z)/r_s(z_d)$, $F_{AP}(z)$ and $f(z)\sigma_8(z)$ are the most precise constraints to date using this technique.

This paper is organized as follows. In Section 2, we describe the BOSS CMASS-DR11 data set. In Section 3, we describe the power spectrum estimator used in our analysis and in Section 4 we describe the mock catalogues together with the derivation of the covariance matrix. We then discuss the measurement of window function effects including the integral constraint in Section 5. In Section 6, we discuss our model for the power spectrum multipoles, together with the modelling of the AP effect. We perform a detailed study of possible systematic uncertainties in Section 7, followed by the data analyses in Section 8. We use our data constraints for cosmological tests in Section 9 and conclude in Section 10. The appendix gives detailed derivations of equations used in our analysis.

The fiducial cosmology used to turn redshifts into distances assumes a flat Λ cold dark matter (Λ CDM) universe with $\Omega_m = 0.3$. The Hubble constant is set to $H_0 = 100 h \text{ km s}^{-1} \text{ Mpc}^{-1}$, with our fiducial model using $h = 0.7$.

2 THE BOSS CMASS-DR11 DATA SET

BOSS, as part of SDSS-III (Eisenstein et al. 2011; Davis et al. 2013), is measuring spectroscopic redshifts of ≈ 1.5 million galaxies (and 150 000 quasars) making use of the SDSS multifibre spectrographs (Bolton et al. 2012; Smee et al. 2013). The galaxies are selected from multicolour SDSS imaging (Fukugita et al. 1996; Gunn et al. 1998; Smith et al. 2002; Gunn et al. 2006; Doi et al. 2010) and cover a redshift range of $z = 0.15\text{--}0.7$, where the survey is split into two samples called LOWZ ($z = 0.15\text{--}0.43$) and CMASS ($z = 0.43\text{--}0.7$). In this analysis, we are only using the CMASS sample. The survey is optimized for the measurement of the BAO scale, and hence covers a large cosmic volume ($V_{\text{eff}} = 2.31 \times 10^9 [\text{Mpc } h^{-1}]^3$) with a density of $\bar{n} \approx 3 \times 10^{-4} [h \text{ Mpc}^{-1}]^3$, high enough to ensure that shot noise is not the dominant error contribution at the BAO scale (White et al. 2011). Most CMASS galaxies are red with a prominent 4000 Å break in their spectral energy distribution. Halo occupation studies have shown that galaxies selected like the CMASS galaxies are mainly central galaxies residing in dark matter haloes of $10^{13} M_\odot h^{-1}$, with a 5–10 per cent satellite fraction (White et al. 2011). CMASS galaxies are highly biased ($b \sim 2$), which boosts the clustering signal including BAO in respect to the shot noise level.

The CMASS-DR11 sample covers 6391 deg² in the North Galactic Cap (NGC) and 2107 deg² in the South Galactic Cap (SGC); the total area of 8498 deg² represents a significant increase from CMASS-DR9, which covered 3265 deg² in total. The sample used in our analysis includes 520 806 galaxies in the NGC and 170 021 galaxies in the SGC. Fig. 2 shows the footprint of the survey in the two regions, where the grey area indicates the expected footprint of DR12.

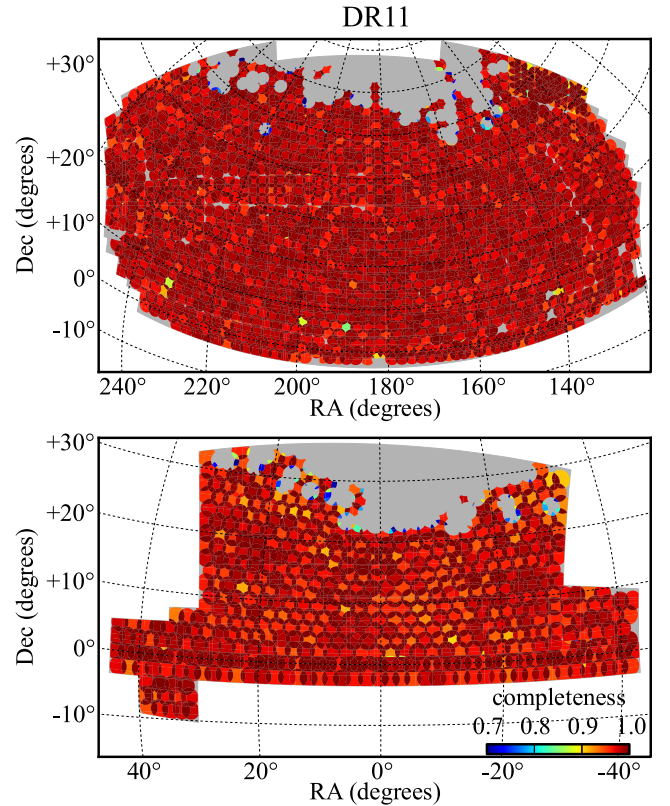


Figure 2. The CMASS-DR11 NGC (top) and SGC (bottom) sky coverage. The grey region indicates the final footprint of the survey (DR12). The colours indicate the completeness in the regions included in our analysis.

We include three different incompleteness weights to account for shortcomings of the CMASS data set (see Ross et al. 2012a; Anderson et al. 2013b for details): a redshift failure weight, w_{rf} , a fibre collision weight, w_{fc} and a systematics weight, w_{sys} , which is a combination of a stellar density weight and a seeing condition weight. Each galaxy is thus coded as

$$w_c = (w_{\text{rf}} + w_{\text{fc}} - 1)w_{\text{sys}}. \quad (1)$$

We will discuss these weights in more detail in Section 3.3.

3 THE POWER SPECTRUM ESTIMATOR

In this section, we describe the power spectrum estimator we use to measure the multipole power spectrum from the CMASS-DR11 sample. We carefully address how to incorporate the incompleteness weights. Before explaining the estimator itself, we summarize different approximations commonly used in galaxy clustering analysis.

3.1 Commonly used approximations

Here, we discuss different approximations used in galaxy clustering statistics, and if used in our analysis we discuss their impact on our measurement as follows.

(i) *Distant observer approximation.* Here one assumes that a displacement Δx (e.g. caused by RSD) is much smaller than the distance, $|x|$, to the galaxy itself. This approximation is commonly used for the volume element in the Jacobian mapping from real to

redshift space. We assume the distant observer approximation when modelling the galaxy power spectrum in Section 6.1.

(ii) *Local plane-parallel approximation.* Here, one assumes that the position vectors of a galaxy pair can be treated as parallel, meaning

$$\hat{\mathbf{k}} \cdot \hat{\mathbf{x}}_1 \approx \hat{\mathbf{k}} \cdot \hat{\mathbf{x}}_2 \approx \hat{\mathbf{k}} \cdot \hat{\mathbf{x}}_h, \quad (2)$$

where $\hat{\mathbf{x}}_h = (\hat{\mathbf{x}}_1 + \hat{\mathbf{x}}_2)/2$ and $\hat{\mathbf{x}} = \mathbf{x}/|\mathbf{x}|$. This approximation is only valid for a galaxy pair with a small angular separation and hence will break down on large scales (Papai & Szapudi 2008). It has been shown, however, that the local plane-parallel approximation is a very good approximation for most galaxy samples even when they cover a large fraction of the sky (Beutler et al. 2011; Samushia, Percival & Raccanelli 2012; Yoo & Seljak 2013). Most of the anisotropic galaxy clustering measurements adopt this assumption including our analysis, where it is introduced in equation (9).

(iii) *(Global) plane-parallel approximation (or flat-sky approximation).* Here, one assumes that the line-of-sight vector $\hat{\mathbf{x}}$ is the same for all galaxies in the survey, meaning

$$\hat{\mathbf{k}} \cdot \hat{\mathbf{x}} \approx \hat{\mathbf{k}} \cdot \hat{\mathbf{z}}, \quad (3)$$

where $\hat{\mathbf{z}}$ is the global line-of-sight vector. This approximation is included in the FKP estimator suggested by Feldman et al. (1994). Since the line-of-sight vector only appears in the calculation of the cosine angle to the line of sight, μ , the monopole power spectrum is not affected by this approximation. The higher order multipoles are strongly affected, except for very narrow angle surveys (Blake et al. 2011a). The invalidity of the plane-parallel approximation for the geometry of the CMASS sample (Yoo & Seljak 2013) motivated the use of the power spectrum estimator suggested by Yamamoto et al. (2006) in our analysis.

3.2 The Yamamoto et al. (2006) power spectrum estimator

The multipole power spectrum of a galaxy distribution can be calculated as (Feldman et al. 1994; Yamamoto et al. 2006)

$$P_\ell(\mathbf{k}) = \frac{(2\ell + 1)}{2A} \left[\int d\mathbf{x}_1 \int d\mathbf{x}_2 F(\mathbf{x}_1)F(\mathbf{x}_2) \times e^{i\mathbf{k} \cdot (\mathbf{x}_1 - \mathbf{x}_2)} \mathcal{L}_\ell(\hat{\mathbf{k}} \cdot \hat{\mathbf{x}}_h) - S_\ell \right], \quad (4)$$

where \mathcal{L}_ℓ is the Legendre polynomial, $\mathbf{x}_h = (\mathbf{x}_1 + \mathbf{x}_2)/2$ and

$$A = \int d\mathbf{x} \left[n'_g(\mathbf{x}) w_{\text{FKP}}(\mathbf{x}) \right]^2, \quad (5)$$

$$F(\mathbf{x}) = w_{\text{FKP}}(\mathbf{x}) \left[n'_g(\mathbf{x}) - \alpha' n_s(\mathbf{x}) \right], \quad (6)$$

where n'_g is the galaxy density, n_s is the density of the random catalogue and α' is the ratio of real galaxies to random galaxies. The shot noise term is given by

$$S_\ell = \int d\mathbf{x} n'_g(\mathbf{x}) w_{\text{sys}}(\mathbf{x}) w_{\text{FKP}}^2(\mathbf{x}) \mathcal{L}_\ell(\hat{\mathbf{k}} \cdot \hat{\mathbf{x}}) + \alpha' \int d\mathbf{x} n'_g(\mathbf{x}) w_{\text{FKP}}^2(\mathbf{x}) \mathcal{L}_\ell(\hat{\mathbf{k}} \cdot \hat{\mathbf{x}}). \quad (7)$$

In our notation, quantities marked with a (') include all incompleteness weights, like $\alpha' = N'_{\text{gal}}/N_{\text{ran}}$ where $N'_{\text{gal}} = \sum_i^{N_{\text{gal}}} (w_{\text{rf}} + w_{\text{fc}} - 1) w_{\text{sys}}$. In CMASS-DR11, the incompleteness weights increase the

average galaxy density by about 8 per cent.¹ Whenever we have to write the weighting explicitly, we use the incompleteness weight $w_c(\mathbf{x}) = (w_{\text{rf}} + w_{\text{fc}} - 1) w_{\text{sys}}$. The random galaxies follow the redshift distribution of the weighted galaxy catalogue, $\langle \alpha' n_s \rangle = \langle n'_g \rangle$, which means that the randoms do not need an incompleteness weight. In addition to the incompleteness weight we employ a minimum variance weight, $w_{\text{FKP}}(\mathbf{x})$, which applies to the data and random galaxies (see equation 21).

Most power spectrum studies in the past employed a fast Fourier transform (FFT) to solve the double integral in equation (4). Such an approach however, requires the (global) plane-parallel approximation (see Section 3 for the definition), which for wide-angle surveys like BOSS, introduces significant bias into the higher order multipoles of the power spectrum (see e.g. Yoo & Seljak 2013). The monopole of the power spectrum is unaffected by this assumption, because it does not require an explicit knowledge of the angle to the line of sight. Yamamoto et al. (2006) suggested a power spectrum estimator which does not use the plane-parallel approximation, for the price of significantly higher computation time. This is the estimator we employ in this analysis.

Using the relation $\int d\mathbf{x} n'_g(\mathbf{x}) \dots \rightarrow \sum_{N_{\text{gal}}} w_c(\mathbf{x}) \dots \rightarrow \alpha' \sum_{N_{\text{ran}}} \dots$, the integrals in equation (4) can be written as

$$F_\ell(\mathbf{k}) = \int d\mathbf{x} F(\mathbf{x}) e^{i\mathbf{k} \cdot \mathbf{x}} \mathcal{L}_\ell(\hat{\mathbf{k}} \cdot \hat{\mathbf{x}}) \quad (8)$$

$$= \sum_i^{N_{\text{gal}}} w_c(\mathbf{x}_i) w_{\text{FKP}}(\mathbf{x}_i) e^{i\mathbf{k} \cdot \mathbf{x}_i} \mathcal{L}_\ell(\hat{\mathbf{k}} \cdot \hat{\mathbf{x}}_i) - \alpha' \sum_i^{N_{\text{ran}}} w_{\text{FKP}}(\mathbf{x}_i) e^{i\mathbf{k} \cdot \mathbf{x}_i} \mathcal{L}_\ell(\hat{\mathbf{k}} \cdot \hat{\mathbf{x}}_i), \quad (9)$$

where the local plane-parallel approximate $\hat{\mathbf{k}} \cdot \hat{\mathbf{x}}_h \approx \hat{\mathbf{k}} \cdot \hat{\mathbf{x}}_i$ has been used. If we define

$$D_\ell(\mathbf{k}) = \sum_i^{N_{\text{gal}}} w_c(\mathbf{x}_i) w_{\text{FKP}}(\mathbf{x}_i) e^{i\mathbf{k} \cdot \mathbf{x}_i} \mathcal{L}_\ell(\hat{\mathbf{k}} \cdot \hat{\mathbf{x}}_i), \quad (10)$$

$$R_\ell(\mathbf{k}) = \sum_i^{N_{\text{ran}}} w_{\text{FKP}}(\mathbf{x}_i) e^{i\mathbf{k} \cdot \mathbf{x}_i} \mathcal{L}_\ell(\hat{\mathbf{k}} \cdot \hat{\mathbf{x}}_i), \quad (11)$$

the power spectrum estimate is given by (Yamamoto et al. 2006; Blake et al. 2011a)

$$P_\ell(\mathbf{k}) = \frac{(2\ell + 1)}{2A} \left[(D_\ell(\mathbf{k}) - \alpha' R_\ell(\mathbf{k})) \times (D_0(\mathbf{k}) - \alpha' R_0(\mathbf{k}))^* - S_\ell \right], \quad (12)$$

where the * represents the complex conjugate. The normalization is given by

$$A = \sum_i^{N_{\text{gal}}} n'_g(\mathbf{x}_i) w_c(\mathbf{x}_i) w_{\text{FKP}}^2(\mathbf{x}_i) \quad (13)$$

$$= \alpha' \sum_i^{N_{\text{ran}}} n'_g(\mathbf{x}_i) w_{\text{FKP}}^2(\mathbf{x}_i) \quad (14)$$

¹ In our analysis, we have $N'_{\text{gal}} = 558\,001$ for the NGC and $N'_{\text{gal}} = 184\,145$ for the SGC, while the actually observed values are $N_{\text{gal}} = 520\,806$ and $170\,021$, respectively.

and the shot noise for each multipole is defined as

$$S_\ell = \sum_i^{N_{\text{gal}}} w_c(\mathbf{x}_i) w_{\text{sys}}(\mathbf{x}_i) w_{\text{FKP}}^2(\mathbf{x}_i) \mathcal{L}_\ell(\hat{\mathbf{k}} \cdot \hat{\mathbf{x}}_i) + \alpha'^2 \sum_i^{N_{\text{ran}}} w_{\text{FKP}}^2(\mathbf{x}_i) \mathcal{L}_\ell(\hat{\mathbf{k}} \cdot \hat{\mathbf{x}}_i). \quad (15)$$

Note that because $\int_{-1}^1 K \mathcal{L}_\ell(\mu) d\mu = 0$ for $\ell > 0$ and any constant K , the shot noise term will vanish for the quadrupole ($\ell = 2$) and hexadecapole ($\ell = 4$) if the window function is isotropic. In order to minimize the additional shot noise contribution from the random catalogue to the power spectrum and its error, we generate a very large (i.e. dense) random catalogue with $\alpha' = 0.036$.

The final power spectrum is then calculated as the average over spherical k -space shells

$$P_\ell(k) = \langle P_\ell(\mathbf{k}) \rangle = \frac{1}{V_k} \int_{k\text{-shells}} d\mathbf{k} P_\ell(\mathbf{k}) \quad (16)$$

$$= \frac{1}{N_{\text{modes}}} \sum_{k - \frac{\Delta k}{2} < |\mathbf{k}| < k + \frac{\Delta k}{2}} P_\ell(\mathbf{k}), \quad (17)$$

where V_k is the volume of the k -space shell and N_{modes} is the number of \mathbf{k} modes in that shell. In our analysis, we use $\Delta k = 0.005 h \text{ Mpc}^{-1}$.

The method described above has a bias at larger scales arising from the discreteness of the gridding in k -space (Blake et al. 2011a). The effect can be estimated by comparing a model power spectrum with a gridded model power spectrum, where the gridded model power spectrum is defined as

$$P_\ell^{\text{gm}}(\mathbf{k}) = \frac{(2\ell + 1)\alpha'}{2A} \sum_{i=1}^{N_{\text{ran}}} n'_g(\mathbf{x}_i) w_{\text{FKP}}^2(\mathbf{x}_i) P^m(k, \mu) \mathcal{L}_\ell(\hat{\mathbf{k}} \cdot \hat{\mathbf{x}}_i). \quad (18)$$

This should be averaged following equation (17) and compared to a model power spectrum of the form

$$P_\ell^{\text{em}}(k) = \frac{(2\ell + 1)}{2} \int_{-1}^1 d\mu P^m(k, \mu) \mathcal{L}_\ell(\mu). \quad (19)$$

The final estimate of the power spectrum is then given by

$$P_\ell^{\text{final}}(k) = P_\ell(k) + P_\ell^{\text{em}}(k) - P_\ell^{\text{gm}}(k), \quad (20)$$

where $P_\ell(k)$ on the right-hand side is the measured power spectrum and $P_\ell^{\text{final}}(k)$ is the measured power spectrum after being corrected for the discrete gridding in k space. In our case, this correction is 0.08 per cent (1.5 per cent) at $k = 0.04 h \text{ Mpc}^{-1}$ and 0.03 per cent (0.09 per cent) at $k = 0.10 h \text{ Mpc}^{-1}$ for the monopole and quadrupole, respectively. We show the measurement of the power spectrum monopole and quadrupole for CMASS-DR11 NGC (black) and SGC (red) in Fig. 3.

3.3 The Poisson shot noise

Here, we are going to discuss the impact of the CMASS incompleteness weighting on the shot noise term. In principle, any arbitrary constant weight applied to observed galaxies should not change the shot noise term, since no information is added. For example if one decides to up-weight each galaxy by a constant factor, e.g. the average incompleteness of the survey, the shot noise term should not change. In CMASS, we have several different kinds of weights, and here we argue that some of these weights use extra information, in a sense that they should reduce the shot noise.

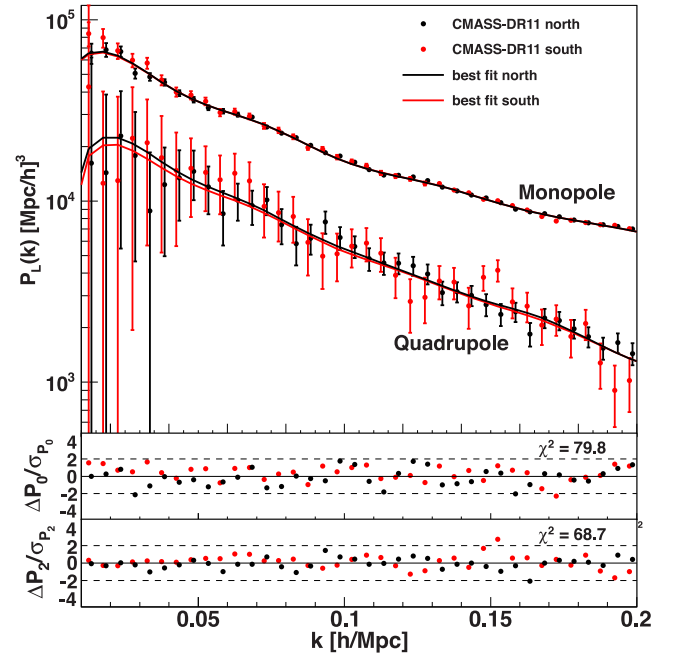


Figure 3. The measured CMASS-DR11 monopole (top) and quadrupole (bottom) power spectra. The black data points are the measurement of the NGC and the red data points are the measurement of the SGC of CMASS-DR11. The black data points have been shifted by $\Delta k = 0.001 h \text{ Mpc}^{-1}$ to the right for clarity. The error bars are the diagonal of the covariance matrix. Because of the smaller volume in the SGC the error bars are larger by a factor of ~ 1.6 . The solid black and red lines represent the best-fitting power spectra for the NGC (black) and SGC (red), respectively (fitting range $k = 0.01\text{--}0.20 h \text{ Mpc}^{-1}$, see Section 8.1). The red and black lines are based on the same cosmology and only differ in the effect of the window function (see Section 5). The lower two panels show the difference between the measured monopole and the best-fitting monopole (middle panel) and the measured quadrupole and the best-fitting quadrupole (bottom panel), both relative to the diagonal elements of the covariance matrix. We fit the monopole and quadrupole simultaneously. The best-fitting χ^2 is $66.6 + 73.9 = 140.5$ (NGC + SGC) for 152 bins and seven free parameters (see Table 2). The contribution to χ^2 from the monopole and quadrupole alone is given in the middle and lower panel, for comparison.

(i) *Fibre collision, w_{fc} and redshift failure, w_{rf} weight:* galaxies which did not get a redshift due to fibre collision or redshift failure are still included in the galaxy catalogue by double counting the nearest galaxy (see Ross et al. 2012a for details). For each missing galaxy we know its angular position exactly. Even though the procedure to use the redshift of the closest galaxy is incorrect for some fraction of the missing galaxies (Guo, Zehavi & Zheng 2012) it means we effectively put extra galaxies into the survey in a non-random fashion, which should reduce the shot noise term. We hence include the fibre collision as well as the redshift failure weights in the shot noise term.

(ii) *Systematic weights, w_{sys} :* the CMASS sample shows correlations between the galaxy density and the proximity to a star as well as between the galaxy density and the seeing conditions for a particular observation. These correlations are removed using galaxy specific weights (systematic weights). Here, we know only statistically that there were missed galaxies, but never know exactly where. To correct for these correlations we up-weight observed galaxies depending on their proximity to stars and the seeing condition for that particular observation. The correction is not random, but it is linked to a Poisson process (e.g. the existence of another galaxy around

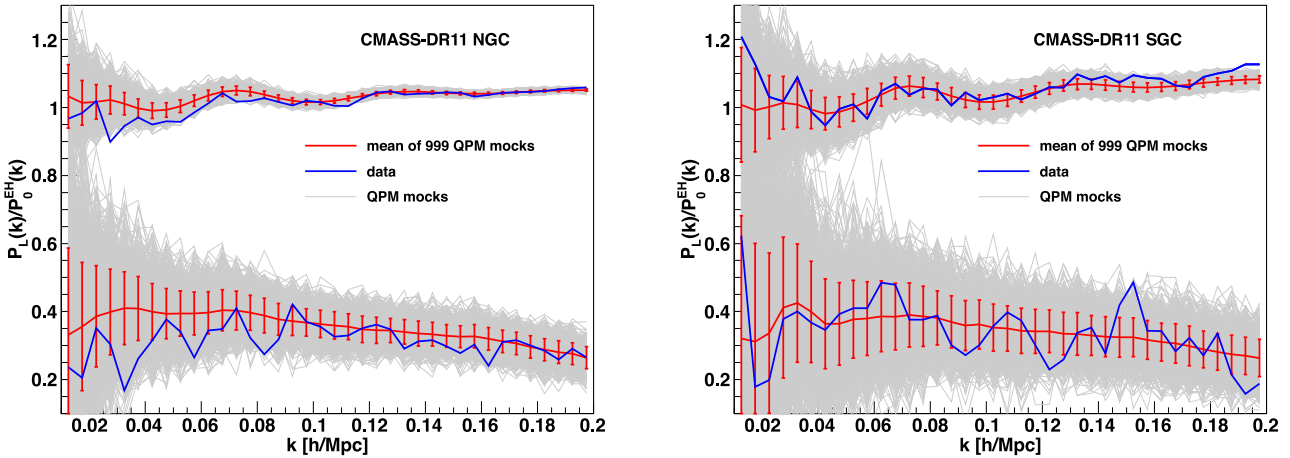


Figure 4. The power spectrum monopole (top) and quadrupole (bottom) of the 999 QPM mock catalogues (grey lines) for the NGC (left) and the SGC (right), relative to an Eisenstein & Hu (1998) no-BAO monopole power spectrum. We plot the power spectrum without the shot noise subtraction, since this way, the scatter closely represents the diagonal of the covariance matrix. The red lines show the mean of all mock catalogues with the error representing the variance around the mean. The blue lines show the measured CMASS-DR11 power spectra.

that star). Therefore, we argue that the systematic weights should not reduce the shot noise. We also note that the systematic weights are much smaller than the fibre collision and redshift failure weight and hence the impact to the shot noise term is small.

The shot noise term defines how the galaxy density field enters in the minimum variance weight, w_{FKP} , and hence the arguments discussed above result in a minimum variance weight of the form:

$$w_{\text{FKP}}(\mathbf{x}) = \frac{1}{1 + \frac{n'_g(\mathbf{x})P_0}{w_{\text{sys}}(\mathbf{x})}}. \quad (21)$$

A detailed derivation can be found in Appendix A. Since the systematic weights employed in our analysis are very small, our definition of w_{FKP} is almost identical to the commonly used

$$w_{\text{FKP}}(\mathbf{x}) = \frac{1}{1 + n'_g(\mathbf{x})P_0}. \quad (22)$$

If we were to assume that the systematic weights, $w_{\text{sys}}(\mathbf{x})$, reduce the shot noise, equations (21) and (22) would be identical. The value of P_0 defines the power spectrum amplitude at which the error is minimized. In this analysis, we use $P_0 = 20\,000 \text{ Mpc}^3 h^{-3}$, which corresponds to $k \sim 0.10 h \text{ Mpc}^{-1}$ and evaluate the density in redshift bins.

Several studies in recent years reported deviations from the pure Poisson shot noise assumption (Casas-Miranda et al. 2002; Seljak, Hamaus & Desjacques 2009; Hamaus et al. 2010; Manera & Gaztanaga 2011; Baldauf et al. 2013). Even though we discussed our definition of the shot noise term at length in this section, the parameter constraints we derive in this paper are fairly independent of the precise definition, since for all parameter constraints we are marginalizing over a constant offset, N (see Section 6.1).

4 CMASS-DR11 MOCK CATALOGUES

In our analysis, we use 999 mock catalogues which follow the same selection function as the CMASS-DR11 sample. The catalogues are produced using quick particle-mesh (QPM) N -body simulations (White, Tinker & McBride 2013) with 1280^3 particles in a $[2560 \text{ Mpc } h^{-1}]^3$ box. These simulations have been found to better describe the clustering of CMASS galaxies compared to the previous version of CMASS mock catalogues (Manera et al. 2012),

especially at small scales (McBride et al., in preparation). Each simulation started from 2LPT initial conditions at $z = 25$ and evolved to the present using time steps of 15 per cent in $\ln(a)$, where $a = (1 + z)^{-1}$ is the scalefactor. The fiducial cosmology assumes flat Λ CDM with $\Omega_m = 0.29$, $h = 0.7$, $n_s = 0.97$ and $\sigma_8 = 0.8$. We use the simulation output at $z = 0.55$, where the simulation generated a subsample of the N -body particles and a halo catalogue using the friends-of-friends algorithm with a linking length of 0.2 times the mean interparticle spacing. The halo catalogue is then extended to lower masses by appointing a set of the subsampled particles as haloes and assigning them a mass using the peak-background split mass function. The haloes are then populated by galaxies using the halo occupation distribution (HOD) formalism with the occupation functions (see e.g. Tinker et al. 2012)

$$\langle N_{\text{cen}} \rangle_M = \frac{1}{2} \left[1 + \text{erf} \left(\frac{\log M - \log M_{\text{min}}}{\sigma_{\log M}} \right) \right], \quad (23)$$

$$\langle N_{\text{sat}} \rangle_M = \langle N_{\text{cen}} \rangle_M \left(\frac{M}{M_{\text{sat}}} \right)^\alpha \exp \left(\frac{-M_{\text{cut}}}{M} \right), \quad (24)$$

where we use $M_{\text{min}} = 9.319 \times 10^{12} M_\odot h^{-1}$, $\sigma_{\log M} = 0.2$, $\alpha = 1.1$, $M_{\text{sat}} = 6.729 \times 10^{13} M_\odot h^{-1}$ and $M_{\text{cut}} = 4.749 \times 10^{13} M_\odot h^{-1}$ (Jeremy Tinker, private communication). In Section 7, we will modify the HOD parameters to test possible systematic effects in our modelling of the power spectrum multipoles. For more details about the QPM mock catalogues see McBride et al. (in preparation) and White et al. (2013).

4.1 The covariance matrix

We measure the power spectrum monopole and quadrupole for each of the 999 QPM mocks, using the estimator introduced in Section 3. The 999 power spectrum monopoles and quadrupoles are shown in Fig. 4 together with the mean (red) and the CMASS-DR11 measurements (blue). We can see that the mock catalogues closely reproduce the data power spectrum multipoles for the entire range of wavenumbers relevant for this analysis.

The covariance matrix is then given by

$$C_{x,y} = \frac{1}{N_s - 1} \sum_{n=1}^{N_s} [P_{\ell,n}(k_i) - \bar{P}_\ell(k_i)] [P_{\ell',n}(k_j) - \bar{P}_{\ell'}(k_j)], \quad (25)$$

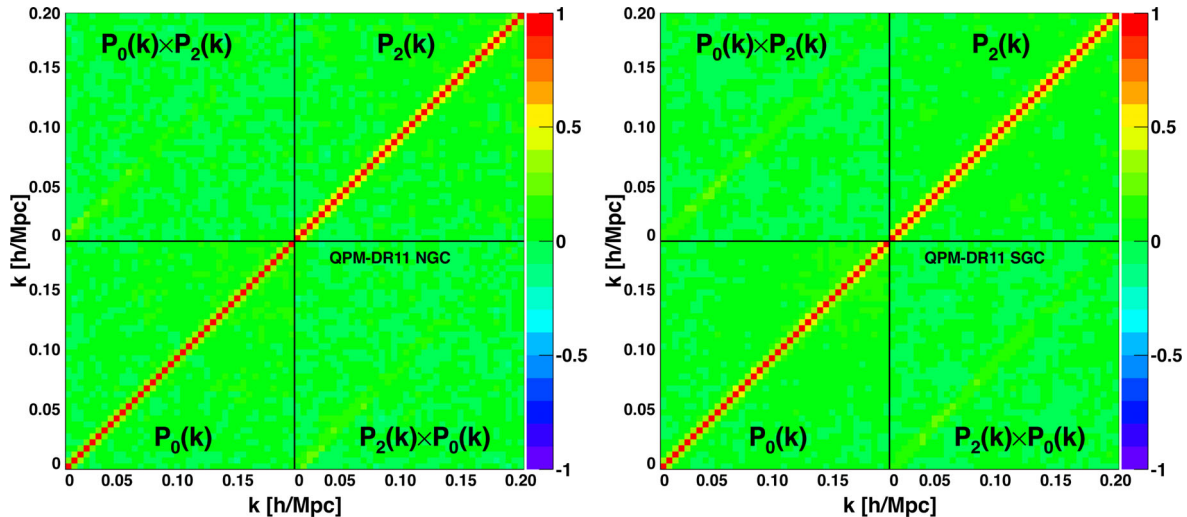


Figure 5. The correlation matrix for the NGC (left) and SGC (right) of CMASS-DR11. The colour indicates the level of correlation, where red represents high correlation, blue represents high anticorrelation and green represents no correlation. The correlation between the bins in the monopole is shown in the lower-left-hand corner, while the correlation between the bins in the quadrupole is shown in the upper-right-hand corner. The upper-left-hand corner and the lower-right-hand corner show the cross-correlations.

where $N_s = 999$ represents the number of mock realizations. We estimate the covariance matrices for the NGC and SGC separately, i.e. treat them as statistically independent samples. This covariance matrix contains the monopole as well as the quadrupole, and the elements of the matrices are given by $(x, y) = (\frac{n_b \ell}{4} + i, \frac{n_b \ell'}{4} + j)$, where n_b is the number of bins in each multipole power spectrum. Our k -binning yields $n_b = 76$ (56) for the fitting range $k_{\max} = 0.01$ – 0.20 (0.01 – 0.15) $h \text{ Mpc}^{-1}$, and hence the dimensions of the covariance matrices become 76×76 (56×56) for the NGC and SGC. The mean of the power spectrum is defined as

$$\bar{P}_\ell(k_i) = \frac{1}{N_s} \sum_{n=1}^{N_s} P_\ell^n(k_i). \quad (26)$$

The mock catalogues automatically incorporate the window function and integral constraint effect present in the data. Fig. 5 shows the correlation matrix for CMASS-DR11 NGC (left) and SGC (right), where the correlation coefficient is defined as

$$r_{xy} = \frac{C_{xy}}{\sqrt{C_{xx}C_{yy}}}. \quad (27)$$

The lower-left-hand corner shows the correlation between bins in the monopole, the upper-right-hand corner shows correlations between the bins in the quadrupole and the upper-left-hand corner and lower-right-hand corner show the correlation between the monopole and quadrupole. Most of the correlation matrix is coloured green, indicating no or a small level of correlation. This is expected for the linear power spectrum since each Fourier mode evolves independently. For larger wavenumbers non-linear effects will introduce correlations between bins, while for very small wavenumbers window function effects can introduce correlations.

As the estimated covariance matrix C is inferred from mock catalogues, its inverse, C^{-1} , provides a biased estimate of the true inverse covariance matrix, due to the skewed nature of the inverse Wishart distribution (Hartlap, Simon & Schneider 2007). To correct for this bias we re-scale the inverse covariance matrix as

$$C_{ij, \text{Hartlap}}^{-1} = \frac{N_s - n_b - 2}{N_s - 1} C_{ij}^{-1}, \quad (28)$$

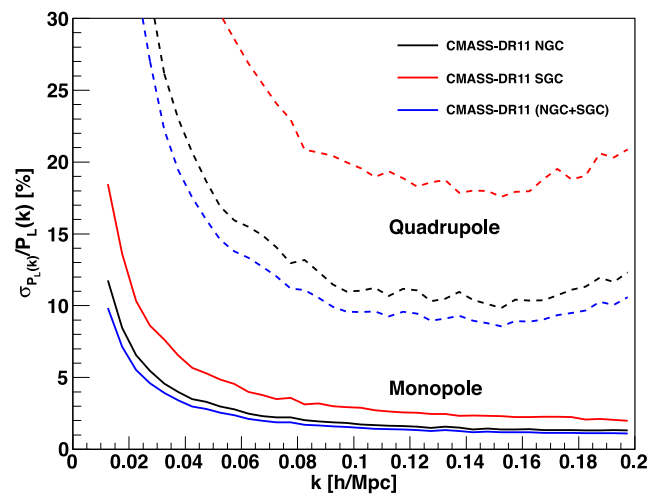


Figure 6. Relative error using the diagonal elements of the covariance matrix of the power spectrum multipoles in CMASS-DR11. The upper three dashed lines show the quadrupole error and the lower three solid lines show the error in the monopole. Because of the larger volume, the error in the NGC of CMASS-DR11 (black lines) is about a factor of 1.6 smaller than the error in the SGC (red lines). The power spectrum error for the entire CMASS-DR11 sample (blue lines) shows an error of ~ 1.5 per cent in the monopole and ~ 10 per cent in the quadrupole at $k = 0.10 h \text{ Mpc}^{-1}$.

where n_b is the number of power spectrum bins. With these covariance matrices we can then perform a standard χ^2 minimization to find the best-fitting parameters.

In Fig. 6, we show the diagonal elements of the covariance matrix for the monopole and quadrupole power spectrum. We find an error of ~ 1.5 per cent in the monopole and ~ 10 per cent in the quadrupole at $k = 0.10 h \text{ Mpc}^{-1}$. This represents the most precise measurement of the galaxy power spectrum multipoles ever obtained.

5 THE SURVEY WINDOW FUNCTION

The power spectrum estimator we discussed in Section 3 is not actually estimating the true galaxy power spectrum, but rather the galaxy

power spectrum convolved with the survey window function:

$$P^{\text{conv}}(\mathbf{k}) = \int d\mathbf{k}' P^{\text{true}}(\mathbf{k}') |W(\mathbf{k} - \mathbf{k}')|^2 - \frac{|W(\mathbf{k})|^2}{|W(0)|^2} \int d\mathbf{k}' P^{\text{true}}(\mathbf{k}') |W(\mathbf{k}')|^2. \quad (29)$$

The window function, $W(\mathbf{k})$ has the following two effects: (1) it mixes the modes with different wavenumbers and introduces correlations and (2) it changes the amplitude of the power spectrum at small k . First we discuss the first term of equation (29), the convolution of the true power spectrum with the window function. The second term of equation (29), the so-called integral constraint, will be discussed in the next subsection. We present the full derivation of the equations of this section in Appendix B and restrict the discussion here to the main results.

5.1 The convolution of the power spectrum with the window function

Window function effects in the measured power spectrum do not necessarily represent a problem, since the survey window function is known in principle. One possible way to handle the window function is to deconvolve the measured power spectrum to get the true galaxy power spectrum (Baugh & Efstathiou 1993; Lin et al. 1996; Sato, Huetsi & Yamamoto 2011; Sato et al. 2013). Here we follow the more common procedure to convolve each model power spectrum (i.e. P^{true}) with the survey window function and derive a model P^{conv} , which is then compared to the measured power spectrum. However, the straightforward implementation of equation (29) mode by mode would lead to a complexity of $\sim \mathcal{O}(N_c^2)$, where N_c is the total number of modes. For most practical cases this is impossible to evaluate. Therefore, most studies in the past evaluated equation (29) as a convolution with the spherically averaged window function, W_s (see e.g. Laix & Starkman 1997; Percival et al. 2001, 2007; Cole et al. 2005; Ross et al. 2012b):

$$P^{\text{conv}}(k) = \int d\epsilon P^{\text{true}}(\mathbf{k} + \epsilon) |W(\epsilon)|_s^2 \quad (30)$$

which assumes an isotropic power spectrum. The spherically averaged window function is defined as

$$|W(\epsilon)|_s^2 = \frac{1}{4\pi} \int d\Omega_{\epsilon'} |W(\epsilon')|^2 \delta(r_{\epsilon'} - r_{\epsilon}), \quad (31)$$

with $r_{\epsilon} = |\mathbf{k} + \epsilon|$. In our analysis, we want to measure anisotropic signals in the power spectrum (AP effect and RSD), and hence the assumption of an isotropic power spectrum seems contradictory.

In a recent analysis, Sato et al. (2013) suggested splitting the survey into subregions (see also Hemantha, Wang & Chuang 2013), which are small enough that the plane-parallel approximation can be applied. In this case, the window function can be calculated using FFTs. However, the window function effect on the power spectrum in any subregion will be larger than in the original survey, and there is a tradeoff between keeping the window function(s) compact and making the plane-parallel approximation work. These problems become especially prominent for the higher order multipoles. In addition to the enhanced window function effects, splitting the survey will discard large-scale modes.

In this section, we will present a treatment of the convolution of the power spectrum with the window function without any assumptions regarding isotropy and without the need to split the survey into subregions. Our approach has a complexity of only $\mathcal{O}(N_{\text{ran}}^2)$. We be-

lieve that our approach is more rigorous and allows a more efficient use of the available data, compared to the methods discussed above.

Since the window function is symmetric around the azimuthal angle ϕ , we can express eq. (29) in terms of wavevector amplitude $k = |\mathbf{k}|$, the cosine of the angle to the line-of-sight μ and the azimuthal angle ϕ :

$$P_{\ell}^{\text{conv}}(k) = \frac{2\ell + 1}{2} \int d\mu \int \frac{d\phi}{2\pi} \int d\mathbf{k}' P^{\text{true}}(\mathbf{k}') |W(\mathbf{k} - \mathbf{k}')|^2 \mathcal{L}_{\ell}(\mu) = 2\pi \int dk' k'^2 \sum_L P_L^{\text{true}}(k') |W(k, k')|_{\ell L}^2, \quad (32)$$

where the window function is now expanded into the Legendre multipole space, and analytical integration over the angles yields

$$|W(k, k')|_{\ell L}^2 = 2i^{\ell} (-i)^L (2\ell + 1) \sum_{ij, i \neq j}^{N_{\text{ran}}} w_{\text{FKP}}(\mathbf{x}_i) w_{\text{FKP}}(\mathbf{x}_j) \times j_{\ell}(k|\Delta\mathbf{x}|) j_L(k'|\Delta\mathbf{x}|) \mathcal{L}_{\ell}(\hat{\mathbf{x}}_i \cdot \Delta\hat{\mathbf{x}}) \mathcal{L}_L(\hat{\mathbf{x}}_j \cdot \Delta\hat{\mathbf{x}}). \quad (33)$$

In this equation, j_{ℓ} represents the spherical Bessel function of order ℓ and $\Delta\mathbf{x} = \mathbf{x}_i - \mathbf{x}_j$ (for a detailed derivation of this equation see Appendix B). We plot the different window function multipoles for CMASS-DR11 in Fig. 7. Equation (33) shows that there are cross terms between different multipoles, meaning that there is a contribution from e.g. the monopole to the convolved quadrupole. In other words, the survey window may induce an anisotropic signal in the convolved power spectrum even without the RSD or AP effect. These cross terms are neglected in the simplified treatment of equation (30).

The normalization for the window function is given by

$$\int d\mathbf{k}' |W(\mathbf{k} - \mathbf{k}')|^2 = 1. \quad (34)$$

In Fig. 8, we show linear model monopole and quadrupole power spectra before (dashed lines) and after (solid lines) the convolution with the CMASS-DR11 window functions. The dotted lines show the convolved monopole power spectra ignoring the quadrupole contribution in equation (32) (black dotted line) and the convolved quadrupole power spectra ignoring the monopole contribution (red dotted line). While the quadrupole contribution to the monopole seems negligible, there is a small monopole contribution to the quadrupole. All window function effects seem quite small in CMASS-DR11, because of the very compact window function. Whether the full treatment of equations (32) and (33) is needed, or whether one of the approximations discussed in the beginning of this section can be employed, needs to be tested for each galaxy survey.

5.2 The integral constraint

Here, we discuss the second term of equation (29). If we go to our original power spectrum estimator (Section 3), we can see that for the mode at $k = 0$ we have by design of the random catalogue:

$$\delta(k = 0) = \sum_i^{N_{\text{gal}}} w_c(\mathbf{x}_i) w_{\text{FKP}}(\mathbf{x}_i) - \alpha' \sum_i^{N_{\text{ran}}} w_{\text{FKP}}(\mathbf{x}_i) = 0. \quad (35)$$

By setting the $k = 0$ mode to zero, we assume that the average density of our survey is equal to the average density of the Universe. The existence of sample variance tells us that this assumption must introduce a bias in our power spectrum estimate, which is known as integral constraint. The effect is that we underestimate the power in modes with wavelength approaching the size of our survey. So

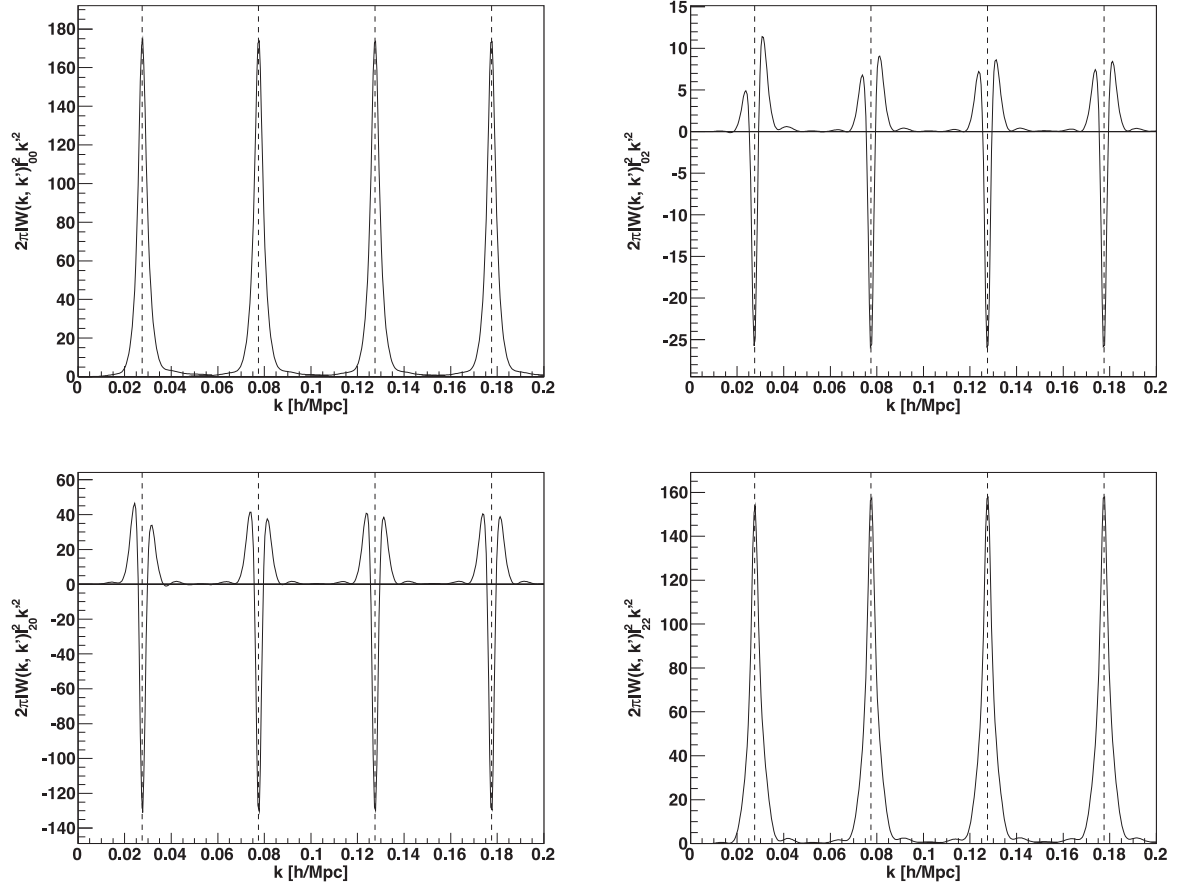


Figure 7. The window function multipoles of the NGC of CMASS-DR11 required in equation (32) and calculated using equation (33). The window function multipoles are plotted as a function of k for fixed values of $k' = (0.0275, 0.0775, 0.1275, 0.1775)$ (black dashed lines). Note that the window function multipoles are not symmetric under ℓ and L (see equation 33).

even neglecting the window function, we do not measure the true underlying power spectrum, but rather a power spectrum with the property $P(k) \rightarrow 0$ for $k \rightarrow 0$ (see e.g. Peacock & Nicholson 1991). This is the reason for the second term in equation (29). It represents the subtraction of the $P(0)$ component which spreads to larger k , because of the convolution with the window function. Similar to what we did with the window function in the last section, we express the second term in eq. (29) in terms of amplitude $k = |\mathbf{k}|$, the cosine of the angle to the line-of-sight μ and the azimuthal angle ϕ :

$$\begin{aligned} P_\ell^{\text{ic}}(k) &= \frac{2\ell + 1}{2} \int d\mu \int \frac{d\phi}{2\pi} \frac{|W(\mathbf{k})|^2}{|W(0)|^2} \\ &\quad \times \left[\int d\mathbf{k}' P^{\text{true}}(\mathbf{k}') |W(\mathbf{k}')|^2 \right] \mathcal{L}_\ell(\mu) \\ &= 2\pi \frac{|W(k)|_\ell^2}{|W(0)|_0^2} \int dk' k'^2 \sum_L P_L^{\text{true}}(k') |W(k')|_L^2 \frac{2}{2L + 1} \end{aligned} \quad (36)$$

with

$$\begin{aligned} |W(k)|_\ell^2 &= i^\ell (2\ell + 1) \sum_{ij, i \neq j}^{N_{\text{ran}}} w_{\text{FKP}}(\mathbf{x}_i) w_{\text{FKP}}(\mathbf{x}_j) \\ &\quad \times j_\ell(k|\Delta\mathbf{x}|) \mathcal{L}_\ell(\hat{\mathbf{x}}_h \cdot \Delta\hat{\mathbf{x}}). \end{aligned} \quad (37)$$

This window function is normalized to

$$4\pi \int dk' k'^2 |W(k')|_0^2 = 1, \quad (38)$$

which is equivalent to equation (34). In Fig. 9, we plot the window function multipoles for the NGC and SGC of CMASS-DR11. The NGC window function multipoles are more compact (concentrated to small k), which results in smaller window function effects in Fig. 8. Later, when we fit the measured power spectrum multipoles, we calculate the integral constraint correction for each model multipole power spectrum and subtract it, following equation (29). This allows a consistent comparison of model power spectra with our measurement.

6 MODELLING THE MULTIPOLE POWER SPECTRA

In this section, we discuss our approach to modelling the multipole power spectra to be compared with the CMASS-DR11 measurement. In order to robustly extract information on RSD and AP from the anisotropic galaxy power spectrum in redshift space, it is crucial to prepare a theoretical template which takes account of the non-linear effects of gravitational evolution, galaxy bias, and RSD at a sufficiently accurate level. Particularly in terms of non-linear RSD, several different approaches to modelling the power spectrum or correlation function of the anisotropic galaxy clustering have been suggested in recent years (Scoccimarro 2004; Matsubara 2008a,b, 2011, 2013; Carlson, White & Padmanabhan 2009; Taruya, Nishimichi & Saito 2010; Reid & White 2011; Seljak & McDonald 2011; Vlah et al. 2012a,b; Blazek et al. 2013; Taruya, Nishimichi & Bernardeau 2013a; Wang, Reid & White 2013).

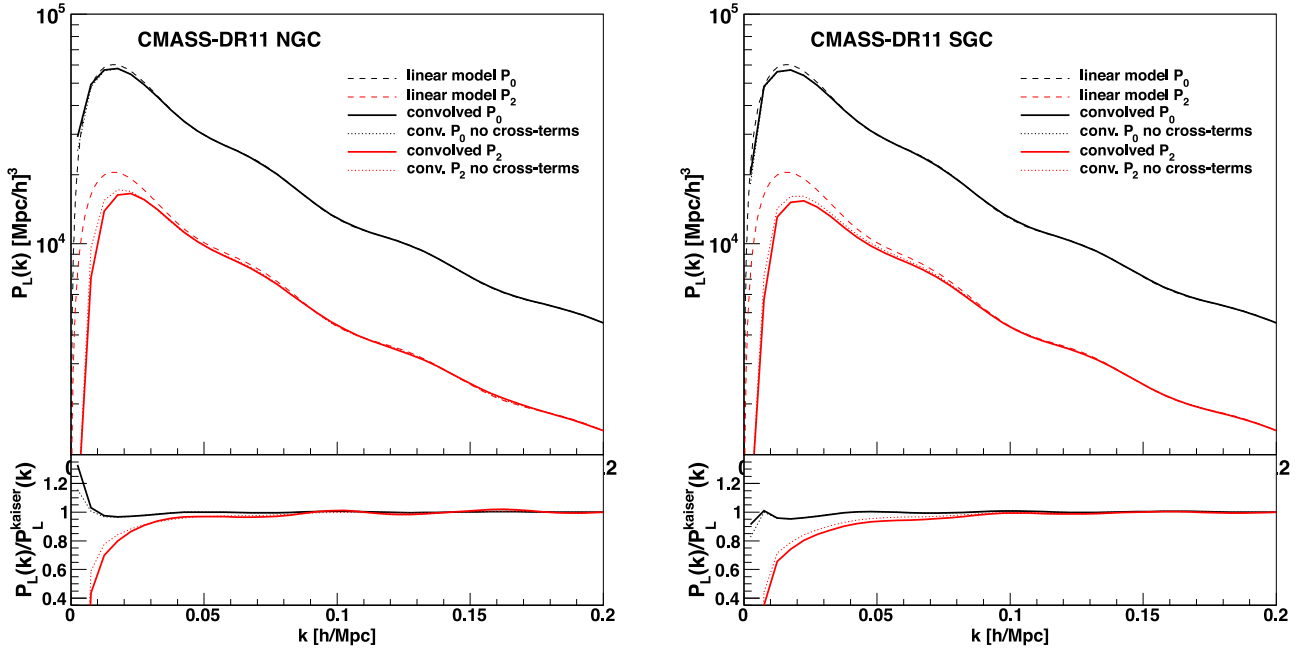


Figure 8. A model monopole (black dashed lines) and quadrupole (red dashed lines) power spectra using Planck cosmological parameters and the linear Kaiser effect. The solid lines show the same models convolved with the CMASS-DR11 window functions for the NGC (left) and the SGC (right). The black dotted lines show the convolved monopole power spectra where the quadrupole contribution to the monopole has been ignored and the red dotted lines show the convolved quadrupole power spectra where the monopole contribution to the quadrupole has been ignored (see equation 32). The bottom panels show the same power spectra relative to the original linear power spectra including the Kaiser effect (dashed lines in the top panels).

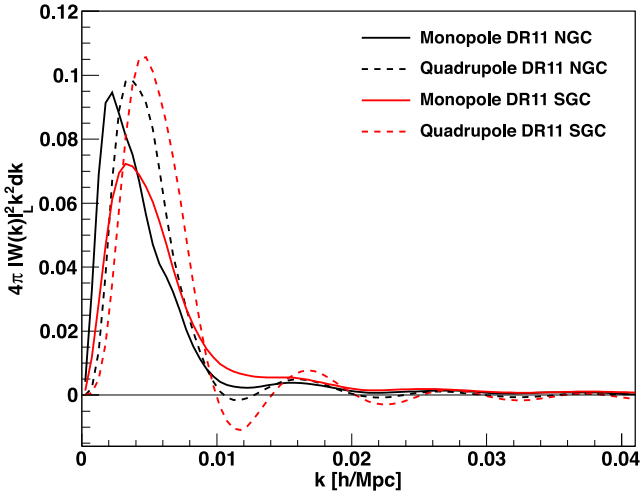


Figure 9. The window function monopole (solid lines) and quadrupole (dashed lines) for the NGC (black lines) and SGC (red lines) calculated using equation (37). The NGC multipoles of CMASS-DR11 peak at smaller wavenumbers k and show weaker oscillations, which is a result of the larger sky coverage (see Fig. 2). The window function multipoles shown in this figure are needed for the integral constraint calculation in equation (36).

We are going to use PT for such non-linear corrections, which is physically well motivated and widely applicable. We first introduce the model of the anisotropic power spectrum in 2D space, and then explain how to incorporate the AP effect.

6.1 PT approach to model the galaxy power spectrum in redshift space

Our model for the anisotropic galaxy power spectrum is based on Taruya et al. (2010):

$$P_g(k, \mu) = \exp\{- (fk\mu\sigma_v)^2\} \left[P_{g,\delta\delta}(k) + 2f\mu^2 P_{g,\delta\theta}(k) + f^2\mu^4 P_{\theta\theta}(k) + b_1^3 A(k, \mu, \beta) + b_1^4 B(k, \mu, \beta) \right], \quad (39)$$

where μ denotes the cosine of the angle between the wavenumber vector and the line-of-sight direction. The overall exponential factor represents the suppression due to the finger of god effect, and we treat σ_v as a free parameter. From now we will call the model in equation (39) extended TNS (eTNS) model.

The first three terms in the square bracket in equation (39) describe an extension of the Kaiser factor. The density ($P_{\delta\delta}$), velocity divergence ($P_{\theta\theta}$) and their cross-power spectra ($P_{\delta\theta}$) are identical in linear theory, while in the quasi non-linear regime, the density power spectrum increases and velocities are randomized on small scales which damps the velocity power spectrum (Scoccimarro 2004). Besides this fact, we need to relate the density and velocity fields for (dark) matter to those of galaxies. Here, we assume no velocity bias, i.e. $\theta_g = \theta$, but include every possible galaxy bias term at next-to-leading order using symmetry arguments (McDonald & Roy 2009):

$$P_{g,\delta\delta}(k) = b_1^2 P_{\delta\delta}(k) + 2b_2 b_1 P_{b_2,\delta}(k) + 2b_{s_2} b_1 P_{b_{s_2},\delta}(k) + 2b_{3nl} b_1 \sigma_3^2(k) P_m^L(k) + b_2^2 P_{b_22}(k) + 2b_2 b_{s_2} P_{b_2 s_2}(k) + b_{s_2}^2 P_{b_{s_2}2}(k) + N, \quad (40)$$

$$P_{g,\delta\theta}(k) = b_1 P_{\delta\theta}(k) + b_2 P_{b_2,\theta}(k) + b_{s_2} P_{b_{s_2},\theta}(k) + b_{3nl} \sigma_3^2(k) P_m^{\text{lin}}(k), \quad (41)$$

where P_m^{lin} is the linear matter power spectrum. Here we introduce five galaxy bias parameters: the renormalized linear bias, b_1 , 2nd-order local bias, b_2 , 2nd-order non-local bias, b_{s_2} , 3rd-order

non-local bias, b_{3nl} , and the constant stochasticity term, N . We evaluate the non-linear matter power spectra, $P_{\delta\delta}$, $P_{\delta\theta}$, $P_{\theta\theta}$ with the REGPT scheme at 2-loop order (Taruya et al. 2012). The other bias terms are given by

$$P_{b_2, \delta}(k) = \int \frac{d^3q}{(2\pi)^3} P_m^{\text{lin}}(q) P_m^{\text{lin}}(|k-q|) F_S^{(2)}(q, k-q), \quad (42)$$

$$P_{b_2, \theta}(k) = \int \frac{d^3q}{(2\pi)^3} P_m^{\text{lin}}(q) P_m^{\text{lin}}(|k-q|) G_S^{(2)}(q, k-q), \quad (43)$$

$$P_{bs_2, \delta}(k) = \int \frac{d^3q}{(2\pi)^3} P_m^{\text{lin}}(q) P_m^{\text{lin}}(|k-q|) \times F_S^{(2)}(q, k-q) S^{(2)}(q, k-q), \quad (44)$$

$$P_{bs_2, \theta}(k) = \int \frac{d^3q}{(2\pi)^3} P_m^{\text{lin}}(q) P_m^{\text{lin}}(|k-q|) \times G_S^{(2)}(q, k-q) S^{(2)}(q, k-q), \quad (45)$$

$$P_{b_{22}}(k) = \frac{1}{2} \int \frac{d^3q}{(2\pi)^3} P_m^{\text{lin}}(q) \left[P_m^{\text{lin}}(|k-q|) - P_m^{\text{lin}}(q) \right], \quad (46)$$

$$P_{b_{2s_2}}(k) = -\frac{1}{2} \int \frac{d^3q}{(2\pi)^3} P_m^{\text{lin}}(q) \left[\frac{2}{3} P_m^{\text{lin}}(q) - P_m^{\text{lin}}(|k-q|) S^{(2)}(q, k-q) \right], \quad (47)$$

$$P_{bs_{22}}(k) = -\frac{1}{2} \int \frac{d^3q}{(2\pi)^3} P_m^{\text{lin}}(q) \left[\frac{4}{9} P_m^{\text{lin}}(q) - P_m^{\text{lin}}(|k-q|) S^{(2)}(q, k-q)^2 \right], \quad (48)$$

where the symmetrized 2nd-order PT kernels, $F_S^{(2)}$, $G_S^{(2)}$, and $S^{(2)}$ are given by

$$F_S^{(2)}(q_1, q_2) = \frac{5}{7} + \frac{q_1 \cdot q_2}{2q_1 q_2} \left(\frac{q_1}{q_2} + \frac{q_2}{q_1} \right) + \frac{2}{7} \left(\frac{q_1 \cdot q_2}{q_1 q_2} \right)^2, \quad (49)$$

$$G_S^{(2)}(q_1, q_2) = \frac{3}{7} + \frac{q_1 \cdot q_2}{2q_1 q_2} \left(\frac{q_1}{q_2} + \frac{q_1}{q_2} \right) + \frac{4}{7} \left(\frac{q_1 \cdot q_2}{q_1 q_2} \right)^2, \quad (50)$$

$$S^{(2)}(q_1, q_2) = \left(\frac{q_1 \cdot q_2}{q_1 q_2} \right)^2 - \frac{1}{3}. \quad (51)$$

If we additionally define

$$D^{(2)}(q_1, q_2) = \frac{2}{7} \left[S^{(2)}(q_1, q_2) - \frac{2}{3} \right], \quad (52)$$

we can write down $\sigma_3^2(k)$ of equation (41) as

$$\sigma_3^2(k) = \frac{105}{16} \int \frac{d^3q}{(2\pi)^3} P_m^{\text{lin}}(q) \left[D^{(2)}(-q, k) S^{(2)}(q, k-q) + \frac{8}{63} \right]. \quad (53)$$

As shown in Chan, Scoccimarro & Sheth (2012) non-linear gravitational evolution naturally induces such non-local bias terms even starting from purely local bias at an initial time. Baldauf et al. (2012) show that the 2nd-order bias is important to explain the large-scale bispectrum in simulations, while the 3rd-order non-local bias terms play a more important role in the power spectrum (Saito et al. 2014). In the case of the local Lagrangian bias picture in which the initial non-local bias is neglected, we can predict the amplitude of the

non-local bias as (Baldauf et al. 2012; Chan et al. 2012; Saito et al. 2014)

$$b_{s_2} = -\frac{4}{7}(b_1 - 1), \quad (54)$$

$$b_{3nl} = \frac{32}{315}(b_1 - 1), \quad (55)$$

which are in good agreement with the values measured in simulations. In this work, we adopt these relations for simplicity, while we float b_1 , b_2 and N as free.² The impact of the 2nd-order bias terms on the power spectrum is somewhat small. Fig. 10 (left) shows the power spectrum multipoles when all higher order bias terms are set to zero (dash-dotted green line). The solid magenta line uses $b_2 = 0.5$ and $b_1 = 2.0$. We can see that the higher order bias terms mainly affect the monopole and while the effect is small, it is significant when compared to the measurement errors (grey shaded area).

We should also mention that the stochastic term, N , can in general depend on scale (Dekel & Lahav 1999; Baldauf et al. 2012), while we treat it as a constant and free parameter. The final ingredients in our model of equation (39) are the correction terms, A and B , which originate from the higher order correlation between Kaiser terms and velocity fields in mapping to redshift space (Taruya et al. 2010). We refer the reader to Taruya et al. (2010) for the definitions of the A and B terms. Note that these terms are in fact proportional to b_1^2 as physically expected if one takes account of $\beta = f/b_1$. Also notice that we drop the 2nd-order bias terms in the A and B correction terms.

6.2 The Alcock–Paczynski effect

If our fiducial cosmological parameters that we use to convert galaxy redshifts into distances deviate from the true cosmology, we artificially introduce an anisotropy in our clustering measurement, which is known as AP distortion (Alcock & Paczynski 1979). This effect can be used to measure cosmological parameters (Ballinger et al. 1996; Matsubara & Suto 1996). To account for the AP effect and its different scaling along and perpendicular to the line-of-sight direction, we can introduce the scaling factors

$$\alpha_{\parallel} = \frac{H^{\text{fid}}(z) r_s^{\text{fid}}(z_d)}{H(z) r_s(z_d)}, \quad (56)$$

$$\alpha_{\perp} = \frac{D_A(z) r_s^{\text{fid}}(z_d)}{D_A^{\text{fid}}(z) r_s(z_d)}, \quad (57)$$

where $H^{\text{fid}}(z)$ and $D_A^{\text{fid}}(z)$ are the fiducial values for the Hubble constant and angular diameter distance at $z = 0.57$ and $r_s^{\text{fid}}(z_d)$ is the fiducial sound horizon assumed in the power spectrum template. The true wavenumbers k'_{\parallel} and k'_{\perp} are then related to the observed wavenumbers by $k'_{\parallel} = k_{\parallel}/\alpha_{\parallel}$ and $k'_{\perp} = k_{\perp}/\alpha_{\perp}$. Transferring this into scalings for the absolute wavenumber $k = \sqrt{k_{\parallel}^2 + k_{\perp}^2}$ and the cosine of the angle to the line of sight μ we can relate the true and observed values by (Ballinger et al. 1996)

$$k' = \frac{k}{\alpha_{\perp}} \left[1 + \mu^2 \left(\frac{1}{F^2} - 1 \right) \right]^{1/2} \quad (58)$$

and

$$\mu' = \frac{\mu}{F} \left[1 + \mu^2 \left(\frac{1}{F^2} - 1 \right) \right]^{-1/2} \quad (59)$$

² We actually vary $b_1 \sigma_8$, $b_2 \sigma_8$ and N , see Section 6.3.

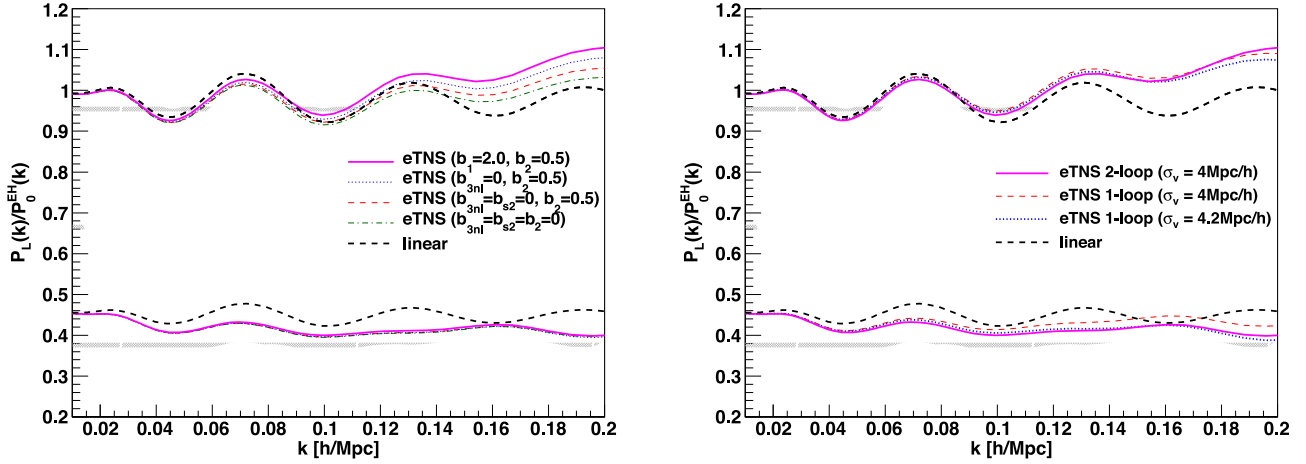


Figure 10. These plots show the effect of different ingredients in the eTNS model (see equation 39). All multipole power spectra are shown relative to an Eisenstein & Hu (1998) no-BAO monopole power spectrum. The black dashed line is the linear CAMB power spectrum, the magenta line is the eTNS model including all correction terms of Section 6.1 and calculating $P_{\delta\delta}$, $P_{\delta\theta}$ and $P_{\theta\theta}$ using 2-loop PT. The grey shaded area along the magenta line shows the 1σ power spectrum errors of CMASS-DR11 (NGC). Left: the dash-dotted green line shows the eTNS model setting $b_2 = 0$, $b_{3nl} = 0$ and $b_{s2} = 0$. The dashed red line and the dotted blue line show the effect of the different bias terms. Right: the dashed red line shows the eTNS model using 1-loop PT and the dotted blue line shows the same model with a different damping σ_v . Comparing the dotted blue line and the solid magenta line, one can see that the difference between 1-loop and 2-loop PT calculation can be absorbed by σ_v to some extent.

with $F = \alpha_{\parallel}/\alpha_{\perp}$. The multipole power spectrum including the AP effect can then be written as

$$P_{\ell}(k) = \frac{(2\ell + 1)}{2\alpha_{\perp}^2 \alpha_{\parallel}} \int_{-1}^1 d\mu P_{\mathbb{g}}(k', \mu') \mathcal{L}_{\ell}(\mu), \quad (60)$$

where we use the eTNS model for $P_{\mathbb{g}}(k', \mu')$. The AP effect constrains the parameter combination $F_{\text{AP}}(z) = (1 + z)D_A(z)H(z)/c$, while the BAO feature constrains the combination $D_V(z)/r_s(z_d) \propto [D_A^2(z)/H(z)]^{1/3}$. Together these two signals allow us to break the degeneracy between $D_A(z)$ and $H(z)$. We will include the scaling parameters α_{\parallel} and α_{\perp} in our model parametrization, which will be discussed in the next section.

6.3 Model parametrization

We parametrize our model using the scaling parameters α_{\parallel} and α_{\perp} introduced in the last section. Using these parameters we can derive

$$\frac{D_V(z_{\text{eff}})}{r_s(z_d)} = \frac{(\alpha_{\perp}^2 \alpha_{\parallel} [(1 + z_{\text{eff}})D_A^{\text{fid}}(z_{\text{eff}})]^2 \frac{c z_{\text{eff}}}{H^{\text{fid}}(z_{\text{eff}})})^{1/3}}{r_s^{\text{fid}}(z_d)} \quad (61)$$

and

$$\begin{aligned} F_{\text{AP}}(z_{\text{eff}}) &= \frac{\alpha_{\perp}}{\alpha_{\parallel}} (1 + z_{\text{eff}}) D_A^{\text{fid}}(z_{\text{eff}}) H^{\text{fid}}(z_{\text{eff}})/c \\ &= (1 + z_{\text{eff}}) D_A(z_{\text{eff}}) H(z_{\text{eff}})/c. \end{aligned} \quad (62)$$

The parameter combination $D_V(z)/r_s(z_d)$ represents the actual quantity which is constrained by the BAO signal, while $F_{\text{AP}}(z)$ is the parameter combination which the AP effect is sensitive to (Padmanabhan & White 2009). Once such geometric parameters are constrained, the relative amplitude of the monopole and quadrupole constrains the growth rate $f(z)\sigma_8(z)$. Beside the three main parameters above (α_{\parallel} , α_{\perp} and $f\sigma_8$), we also include four nuisance parameters in our power spectrum model: the power spectrum amplitudes, $b_1\sigma_8(z_{\text{eff}})$ and $b_2\sigma_8(z_{\text{eff}})$, the velocity dispersion σ_v and the shot noise component N .

Any use of the parameter constraints from this analysis should take into account the underlying assumption of our analysis. We assume that the measured Planck cosmology at very high redshift can be used to build the ‘initial condition’ for the linear clustering amplitude on which our power spectrum model, including all non-linear corrections, is based.

6.4 Effective wavenumber

In our introduction, we advertized RSD as one probe which is able to test GR on very large scales. So what is the scale of our measurement? The information covariance, $C_{ij,\text{info}}^{-1}$ can be calculated as

$$C_{ij,\text{info}}^{-1} = \sum_{\ell\ell'} \frac{d \ln P_{\ell}(k_i)}{df\sigma_8} C_{ij,\text{Hartlap}}^{-1} \frac{d \ln P_{\ell'}(k_j)}{df\sigma_8}, \quad (63)$$

where P_{ℓ} is the eTNS model power spectrum we introduced in Section 6.1 and $C_{ij,\text{Hartlap}}^{-1}$ is the covariance matrix we derived in Section 4. We now can calculate the effective wavenumber as

$$k_{\text{eff}} = \sqrt{\frac{1}{A} \sum_{i,j} k_i C_{ij,\text{info}}^{-1} k_j}. \quad (64)$$

Here, the normalization A is given by $A = \sum_{ij} C_{ij,\text{info}}^{-1}$. Using $k_{\text{max}} = 0.20 \text{ h Mpc}^{-1}$ we get $k_{\text{eff}} = 0.178 \text{ h Mpc}^{-1}$, which can be related to a real-space scale by $s = 1.15\pi/k_{\text{eff}} \approx 20.3 \text{ Mpc h}^{-1}$ (Reid & White 2011). The effective wavenumber of our measurement using $k_{\text{max}} = 0.15 \text{ h Mpc}^{-1}$ is $k_{\text{eff}} = 0.132 \text{ h Mpc}^{-1}$.

7 TESTING FOR SYSTEMATIC UNCERTAINTIES AND DETERMINING THE MAXIMUM WAVENUMBER, k_{max}

The question of the maximum wavenumber, k_{max} up to which we can trust our power spectrum model, is directly linked to the question of possible systematic uncertainties. We would like to make use of as much data as possible, but there are significant power spectrum modelling issues given the small error bars of our measurement.

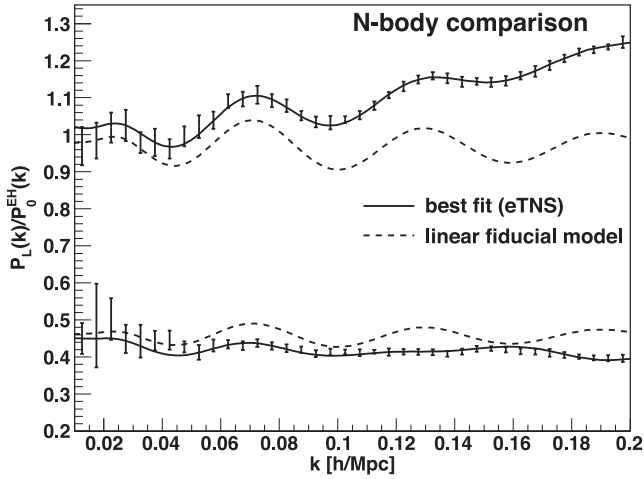


Figure 11. The power spectrum monopole (top) and quadrupole (bottom) measured in a set of N -body simulations (black data points) plotted relative to the fiducial Eisenstein & Hu (1998) no-BAO monopole power spectrum. The solid black line represents the best-fitting model. The fitting range is $k = 0.01\text{--}0.20 h \text{Mpc}^{-1}$. The error at each data point is the variation between the 20 simulation boxes covering a total volume of $67.5 [\text{Gpc } h^{-1}]^3$.

7.1 Test with N -body simulation

To test whether our power spectrum model can extract the correct cosmological parameters from a power spectrum measurement, we use a set of 20 N -body simulations described in White et al. (2011) that were generated using a TreePM code. The simulations cover a total volume of $67.5 [\text{Gpc } h^{-1}]^3$. Note, that we use these N -body simulations only for this subsection and use the QPM simulations for the rest of this paper. We calculate the monopole and quadrupole power spectrum for these simulations and perform a fit using our power spectrum model. When using the fitting range $k = 0.01\text{--}0.20 h \text{Mpc}^{-1}$, the best-fitting value of $f(z_{\text{eff}})\sigma_8(z_{\text{eff}})$ deviates from the fiducial value of the simulation by 3.1 per cent, while we cannot find any significant deviation for α_{\parallel} and α_{\perp} . A comparison between the model and the measured power spectrum in these N -body simulations can be seen in Fig. 11. Using $k_{\text{max}} = 0.15 h \text{Mpc}^{-1}$ we find deviations of -0.1 , -0.1 and -0.7 per cent for α_{\parallel} , α_{\perp} and $f(z_{\text{eff}})\sigma_8(z_{\text{eff}})$, respectively. We include these values in Table 1 and Fig. 12.

Several authors have recently performed similar studies to what we have done here (Nishimichi & Taruya 2011; de la Torre & Guzzo 2012; Ishikawa et al. 2013; Oka et al. 2013). They studied the systematic uncertainty against haloes (or subhaloes) in N -body simulations using the Taruya, Nishimichi & Saito (2010) model. Although some of these studies ignore the AP effect, which is

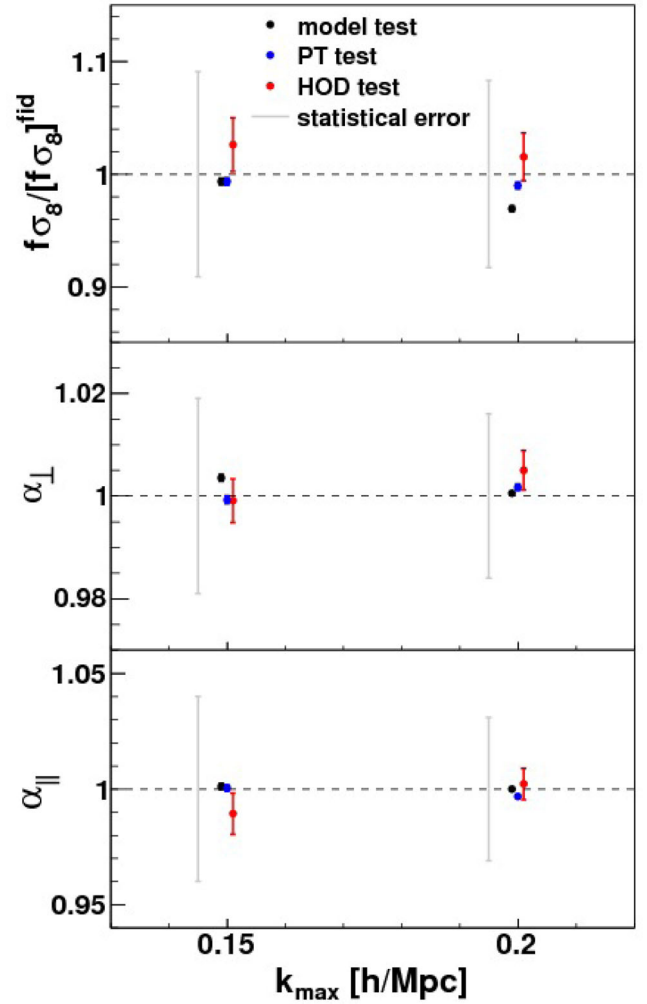


Figure 12. The best-fitting values for α_{\parallel} , α_{\perp} and $f\sigma_8/[f\sigma_8]^{\text{fid}}$ for the different systematic tests performed in this analysis using the fitting range $k = 0.01\text{--}0.15$ and $0.01\text{--}0.20 h \text{Mpc}^{-1}$. The data points have been shifted away slightly from $k_{\text{max}} = 0.15$ and $0.20 h \text{Mpc}^{-1}$ for clarity. The black data points are obtained from the comparison with N -body simulations (see Section 7.1), the blue data points show the result when using 1-loop PT (see Section 7.2) and the red data points show the result when varying the underlying HOD (see Section 7.3). For this plot, we restrict ourselves to the case $M_{\text{sat}} - 1\sigma = 5 \times 10^{13} M_{\odot} h^{-1}$, which has the largest deviation from the CMASS HOD. The PT test used the mean of the 999 QPM mocks and has error bars of a factor of $\sim\sqrt{999}$ smaller than the plotted statistical error (grey line). The HOD tests have been performed on the mean of 20 mock catalogues and hence have errors $\sim\sqrt{20}$ smaller than the statistical errors.

Table 1. Summary of systematic uncertainties of α_{\parallel} , α_{\perp} and $f(z_{\text{eff}})\sigma_8(z_{\text{eff}})$. The shift parameters α_{\parallel} and α_{\perp} are closely related to $H(z_{\text{eff}})$ and $D_A(z_{\text{eff}})$, respectively. The different lines in this table are as follows. Comparison to N -body simulations (see Section 7.1), comparison between 1-loop and 2-loop PT (see Section 7.2) and varying the underlying HOD (see Section 7.3). In the case of the HOD test, we include the result for $M_{\text{sat}} - 1\sigma = 5 \times 10^{13} M_{\odot} h^{-1}$, which represents the largest variation compared to the CMASS HOD. We find significant systematic uncertainties only for $f(z_{\text{eff}})\sigma_8(z_{\text{eff}})$. Based on these uncertainties we chose $k_{\text{max}} = 0.20 h \text{Mpc}^{-1}$, since this is where the error on $f(z_{\text{eff}})\sigma_8(z_{\text{eff}})$ is minimized (using the quadrature sum of the statistical and the largest systematic error). For comparison in the last row we included the expected statistical uncertainty for each parameter with different k_{max} , which we obtained by fitting the mean of the 999 mock catalogues using the data covariance matrix.

Source	$\alpha_{\parallel} [H(z_{\text{eff}})]$		$\alpha_{\perp} [D_A(z_{\text{eff}})]$		$f(z_{\text{eff}})\sigma_8(z_{\text{eff}})$		
	$k_{\text{max}} [h \text{Mpc}^{-1}]$	0.15	0.20	0.15	0.20	0.15	0.20
Model test		0.11 ± 0.13 per cent	0.00 ± 0.10 per cent	0.352 ± 0.061 per cent	0.052 ± 0.049 per cent	-0.66 ± 0.29 per cent	-3.08 ± 0.26 per cent
PT test		0.04 ± 0.14 per cent	-0.32 ± 0.12 per cent	-0.075 ± 0.074 per cent	0.168 ± 0.060 per cent	-0.65 ± 0.33 per cent	-1.01 ± 0.30 per cent
HOD test		-1.07 ± 0.89 per cent	0.21 ± 0.67 per cent	-0.09 ± 0.42 per cent	0.50 ± 0.38 per cent	2.6 ± 2.4 per cent	1.5 ± 2.1 per cent
Statistical error		4.0 per cent	3.1 per cent	1.9 per cent	1.6 per cent	9.1 per cent	8.3 per cent

degenerate with $f\sigma_8$ and use a phenomenological treatment of the galaxy/halo bias, they reach very similar conclusions.

7.2 Uncertainties from perturbation theory

Because we want to make use of the power spectrum beyond $k = 0.10 h \text{Mpc}^{-1}$ we cannot rely on standard PT which seems to break down at low redshift for $k > 0.10 h \text{Mpc}^{-1}$, where the 2-loop term turns out to be larger than the 1-loop term (Crocce & Scoccimarro 2006; Carlson et al. 2009; Taruya et al. 2009). We therefore use re-normalized PT to calculate $P_{\delta\delta}$, $P_{\theta\theta}$ and $P_{\delta\theta}$ (Taruya & Hirata 2008; Taruya et al. 2009, 2013a) and include corrections up to 2-loop order. We make use of the publicly available REGPT code (Taruya et al. 2012).

The authors of this code suggested a phenomenological rule for the maximum wavenumber up to which the model is numerically stable, which they call k_{crit} given by

$$\frac{k_{\text{crit}}^2}{6\pi^2} \int_0^{k_{\text{crit}}} dk P_{\text{m}}^{\text{lin}}(k) = 0.7. \quad (65)$$

This rule is roughly based on percent level accuracy. At redshift $z_{\text{eff}} = 0.57$ with a Planck cosmological model we get $k_{\text{crit}} = 0.28 h \text{Mpc}^{-1}$.

To get a rough upper limit on the effect of ignoring terms higher than 2nd order, we estimate the effect of ignoring the 2nd-order term since we expect that the effect of the former is smaller than the latter. We therefore calculate the power spectra at 1-loop order and measure the amplitude differences of the power spectra at different wavenumbers. We find $\Delta P_{\delta\delta}$ of (0.5, 0.2, 3.2) per cent at $k = (0.10, 0.15, 0.20) h \text{Mpc}^{-1}$. The corresponding values for $\Delta P_{\delta\theta}$ are (3.4, 5.2, 4.8) per cent and for $\Delta P_{\theta\theta}$ we find (6.3, 10.3, 12.2) per cent. While these differences seem very significant, we are actually only interested in the bias these uncertainties introduce in our cosmological parameters. We use the 1-loop power spectra calculated from REGPT instead of the 2-loop power spectra and build our model following Section 6.1. We then fit this model to the mean of the 999 QPM mock power spectra. The shifts in the cosmological parameters are shown in Table 1 and Fig. 10 (right). We see a shift of 1.0 per cent in $f(z_{\text{eff}})\sigma_8(z_{\text{eff}})$ when using the fitting range $k = 0.01\text{--}0.20 h \text{Mpc}^{-1}$, while the shifts in α_{\parallel} and α_{\perp} are much smaller.

Fig. 10 (right) shows the eTNS model using 2-loop and 1-loop PT. The 1-loop case has a larger amplitude in the quadrupole, while the monopole is much less affected. The differences in the quadrupole are caused mainly by the big changes in $P_{\theta\theta}$ going from the 2-loop to 1-loop calculation. Most of the difference can be absorbed by nuisance parameters like σ_v . This is also included in Fig. 10 (right) as the dotted blue line, where we use the 1-loop calculations, but changed σ_v from 4.0 to $4.2 \text{Mpc} h^{-1}$ bringing the model in good agreement with the 2-loop calculation (solid magenta line). Therefore, σ_v can absorb the difference between 1-loop and 2-loop calculation to a great extent, which is the reason why the large difference in the power spectrum amplitude does not transfer into large differences in the actual parameter constraints.

7.3 The impact of different HODs

Here, we want to test how sensitive our power spectrum model is to the underlying HOD. Ideally one would want to constrain the HOD parameters together with the cosmological parameters, by using all information in the galaxy clustering, down to very small scales. However, current model uncertainties do not allow such studies.

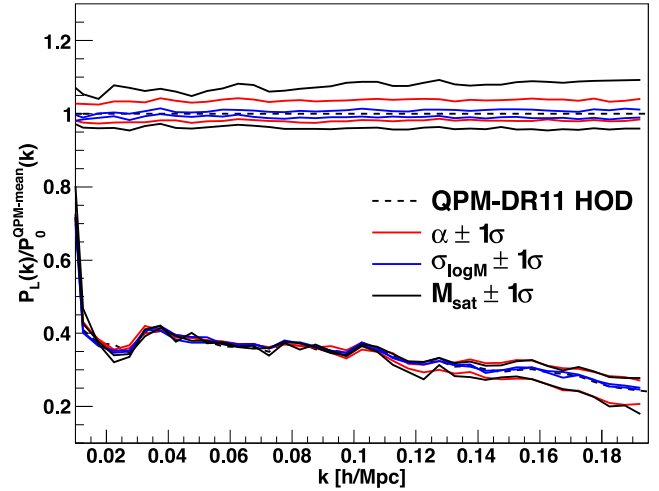


Figure 13. We plot the mean of the power spectrum monopole and quadrupole measured from 20 CMASS mock catalogues with varying HOD relative to the power spectrum monopole using the fiducial HOD parametrization of Section 4. The red lines show the power spectrum multipoles where we varied α (see Section 7.3 for details) while the blue and black lines show variations in $\sigma_{\log M}$ and M_{sat} , respectively.

The CMASS-DR11 mock catalogues which we introduced in Section 4 are populated with a specific HOD model. The question is, whether our ability to extract the correct cosmological parameters does depend on this HOD?

To test this, we create CMASS-DR11 catalogues, based on the same original simulation box as the mock catalogues used in Section 4, but populated with different HODs. We vary the three HOD parameters ($\sigma_{\log M}$, α and M_{sat}) by the 1σ uncertainties reported in White et al. (2011). The explicit variations are $\sigma_{\log M} = 0.04$, $\sigma_{\alpha} = 0.2$ and $\sigma_{M_{\text{sat}}} = 1.3 \times 10^{13} M_{\odot} h^{-1}$, meaning we generate six different HOD models. We choose M_{min} so that the number density is kept fixed. Because White et al. (2011) used a data set about 10 times smaller than CMASS-DR11, the real uncertainties on the HOD parameters should be significantly smaller. For each new set of HOD parameters we create 20 mock catalogues. We calculate the mean of the 20 power spectra and fit our model to it. We show the power spectrum monopole and quadrupole for the different HODs in Fig. 13. As expected, different HODs mainly affect the amplitude of the monopole, but do not cause significant changes in the shape even at $k = 0.20 h \text{Mpc}^{-1}$.

All parameter fits result in constraints on α_{\parallel} , α_{\perp} and $f(z)\sigma_8(z)$ in good agreement with the original HOD parametrization (black dashed line in Fig. 13). Since we are only fitting the mean of 20 mock catalogues for each HOD model, we are only sensitive to shifts ~ 5 times smaller than our measurement uncertainties.³ However, we consider this level of accuracy to be sufficient for the purpose of this analysis. We include the result for $M_{\text{sat}} - 1\sigma = 5 \times 10^{13} M_{\odot} h^{-1}$ in Table 1 and Fig. 12, since this is where we find the largest deviation from the CMASS HOD.

RSDs are induced by the peculiar velocities which are assumed to follow the underlying dark matter field. Violations of this assumption are usually called velocity bias. In our analysis we do not consider the issues related to the velocity bias, which could have a non-negligible impact. We here simply assume that the galaxies

³ Since we are using the same cosmic volume as in the original mock catalogues our sensitivity is a little bit better than just a factor of 5.

Table 2. The maximum likelihood and mean together with the 1σ error for the main cosmological parameters (first 3 rows), the 4 nuisance parameters (middle 4 rows) as well as several derived parameters (last 7 rows). While we report the results for two different fitting ranges, we regard the results for the fitting range $k = 0.01\text{--}0.20 \text{ h Mpc}^{-1}$ as the main results of this work. Our measurements have an effective redshift of $z_{\text{eff}} = 0.57$. The effective wavenumber is $k_{\text{eff}} = 0.132 \text{ h Mpc}^{-1}$ when using $k_{\text{max}} = 0.15 \text{ h Mpc}^{-1}$ and $k_{\text{eff}} = 0.178 \text{ h Mpc}^{-1}$ when using $k_{\text{max}} = 0.20 \text{ h Mpc}^{-1}$ (see Section 6.4). The best-fitting $\chi^2/\text{d.o.f.}$ is $90.3/(112 - 7)$ and $140.5/(152 - 7)$ when using the smaller and larger fitting range, respectively. We include the systematic error on $f\sigma_8$ for the larger fitting range (note that the systematic error has to be added in quadrature, resulting in $f(z_{\text{eff}})\sigma_8(z_{\text{eff}}) = 0.419 \pm 0.044$). The last three rows of the table contain the derived parameter $\beta = f(z_{\text{eff}})\sigma_8(z_{\text{eff}})/[b_1\sigma_8(z_{\text{eff}})]$, as well as the bias parameters b_1 and b_2 . To derive the bias parameters we assumed a fiducial $\sigma_8^{\text{fid}}(z = 0) = 0.80$. Since the cosmological parameters included in this table are correlated, we recommend using the multivariate Gaussian likelihood presented in Section 8.3.

Fitting range	0.01–0.15 $h \text{ Mpc}^{-1}$		0.01–0.20 $h \text{ Mpc}^{-1}$	
	Best fit	Mean $\pm 1\sigma$	Best fit	Mean $\pm 1\sigma$
α_{\parallel}	1.008	1.005 ± 0.057	1.014	1.018 ± 0.036
α_{\perp}	1.026	1.029 ± 0.023	1.029	1.029 ± 0.015
$f(z_{\text{eff}})\sigma_8(z_{\text{eff}})$	0.420	0.423 ± 0.052	0.422	$0.419 \pm (\overset{\text{stat}}{0.042} + \overset{\text{sys}}{0.014})$
$b_1\sigma_8(z_{\text{eff}})$	1.221	1.222 ± 0.044	1.221	1.224 ± 0.031
$b_2\sigma_8(z_{\text{eff}})$	1.7	0.7 ± 1.2	−0.21	$−0.09 \pm 0.62$
σ_v	$4.6 \text{ Mpc } h^{-1}$	$4.3 \pm 1.3 \text{ Mpc } h^{-1}$	$4.63 \text{ Mpc } h^{-1}$	$4.65 \pm 0.81 \text{ Mpc } h^{-1}$
N	$1030 [\text{Mpc } h^{-1}]^3$	$1080 \pm 620 [\text{Mpc } h^{-1}]^3$	$1890 [\text{Mpc } h^{-1}]^3$	$1690 \pm 600 [\text{Mpc } h^{-1}]^3$
$D_V(z_{\text{eff}})/r_s(z_d)$	13.83	13.85 ± 0.27	13.88	13.89 ± 0.18
$F_{\text{AP}}(z_{\text{eff}})$	0.684	0.686 ± 0.046	0.683	0.679 ± 0.031
$H(z_{\text{eff}})r_s(z_d)/r_s^{\text{fid}}(z_d)$	$94.0 \text{ km s}^{-1} \text{ Mpc}^{-1}$	$94.1 \pm 5.4 \text{ km s}^{-1} \text{ Mpc}^{-1}$	$93.5 \text{ km s}^{-1} \text{ Mpc}^{-1}$	$93.1 \pm 3.3 \text{ km s}^{-1} \text{ Mpc}^{-1}$
$D_A(z_{\text{eff}})r_s^{\text{fid}}(z_d)/r_s(z_d)$	1385 Mpc	$1389 \pm 31 \text{ Mpc}$	1389 Mpc	$1388 \pm 22 \text{ Mpc}$
β	0.344	0.346 ± 0.043	0.346	0.342 ± 0.037
$b_1 \times (0.8/\sigma_8)$	2.035	2.037 ± 0.073	2.035	2.040 ± 0.052
$b_2 \times (0.8/\sigma_8)$	2.8	1.2 ± 2.0	−0.4	$−0.2 \pm 1.0$

follow the velocity field of dark matter haloes. There are various scenarios that could affect the galaxy peculiar velocity field, such as the velocity bias related to the peak formation (Bardeen et al. 1986; Desjacques & Sheth 2010), the offset of the central galaxies (Hikage, Takada & Spergel 2012a; Hikage et al. 2012b; Hikage & Yamamoto 2013) and the kinematical features of the satellite galaxies (Masaki et al. 2013; Nishimichi & Oka 2013). These issues are beyond the scope of this paper and should be addressed using the galaxy clustering or the galaxy–galaxy lensing signal at somewhat smaller scales where the 1-halo term is more dominant (for CMASS see Miyatake et al. 2013; Reid et al. 2014). Nevertheless, we believe that our results should be fairly robust against such effects, since we do not confirm any significant differences when changing the fitting range (see Table 2 and the discussion in Section 8.2).

7.4 Uncertainty in the underlying linear matter power spectrum

The BOSS data set, like all galaxy redshift survey data sets, cannot constrain all ΛCDM parameters just by itself, due to parameter degeneracies. Our analysis therefore makes use of the information coming from the analysis of the CMB, in a sense that we take the cosmological parameters found in Planck and use them as initial conditions. We then test whether such initial conditions lead to the clustering signal measured with our data set. In our model, we are using a power spectrum with fixed cosmological parameters. The assumption here is that the Planck uncertainty in most of the parameters which define the shape of the power spectrum is much smaller than the uncertainty of our measurement and hence can be neglected. This assumption has been found to be reasonable for the CMASS-DR9 data set combined with *Wilkinson Microwave Anisotropy Probe 7* (WMAP7; Reid et al. 2012). We repeat the test of Reid et al. (2012), where we only consider the Planck uncertainty

in $\omega_c = \Omega_c h^2$, representing the least well-constrained parameter important for our analysis. We then calculate the quantity

$$s = \frac{\Delta p}{\Delta \omega_c} \frac{\sigma_{\omega_c}}{\sigma_p}, \quad (66)$$

where Δp stands for the change in our parameter constraint when changing ω_c by $\Delta \omega_c$ and σ_p is the uncertainty in the parameter p at fixed ω_c . The uncertainty in p when marginalized over ω_c is increased by $\sqrt{1 + s^2}$ assuming Gaussian probability distribution functions. By fitting the mean of the 999 mock catalogues and using the fitting range $k = 0.01\text{--}0.20 \text{ h Mpc}^{-1}$ we find $\sigma_p = (0.031, 0.016, 0.038)$ for α_{\parallel} , α_{\perp} and $f(z_{\text{eff}})\sigma_8(z_{\text{eff}})$, respectively. For $\Delta \omega_c = 0.02$ we find $\Delta \alpha_{\parallel} = 0.015$, $\Delta \alpha_{\perp} = 0.016$ and $\Delta f(z_{\text{eff}})\sigma_8(z_{\text{eff}}) = 0.008$ leading to $s = 0.07$, $s = 0.14$ and $s = 0.03$, respectively. These results imply that the error in α_{\perp} would increase by only 1.0 per cent if the Planck errors are propagated to our results while the effect on α_{\parallel} and $f(z_{\text{eff}})\sigma_8(z_{\text{eff}})$ is even smaller. These uncertainties are negligible and justify our choice to fix these parameters in our analysis. As a further test we changed the power spectrum template from the fiducial cosmology to a different one, varying the cosmological parameters within the WMAP9 uncertainties and find that the best-fitting values changed by <0.1 per cent.

7.5 Summary of the study of possible systematics

Table 1 and Fig. 12 summarize the results of our systematics test. Since the systematic errors we found are related, we use only the largest systematic error and combine it with the statistical error (in quadrature). We only find significant systematic bias for $f\sigma_8$ when using the larger fitting range of $k = 0.01\text{--}0.20 \text{ h Mpc}^{-1}$, given by 3.1 per cent. For all other parameters as well as for the smaller fitting range of $k = 0.01\text{--}0.15 \text{ h Mpc}^{-1}$, we did not find any significant systematic errors. Since $f\sigma_8$ is the parameter of interest for this analysis, we chose the maximum wavenumber according to where the total

error of $f\sigma_8$ is minimized. This is the case at $k_{\max} = 0.20 h \text{ Mpc}^{-1}$. We did not test wavenumbers beyond $k = 0.20 h \text{ Mpc}^{-1}$. Note, that the geometric parameters α_{\parallel} and α_{\perp} are more robust against systematic errors and could go to larger wavenumbers when marginalizing over $f(z_{\text{eff}})\sigma_8(z_{\text{eff}})$. Such an analysis can be found in Anderson et al. (2013b) and if only the geometric information is needed, we recommend using the constraints quoted in this analysis. Note however, that the extra information contained in the growth rate can lead to substantially improved constraints even for geometric parameters, like the dark energy equation of state w (Rapetti et al. 2012; Reid et al. 2012; Chuang et al. 2013a).

There are other aspects of galaxy clustering which we did not investigate here, which could also introduce systematic biases into our measurement. Naturally, our analysis has to be interpreted with respect to the tests made in this section.

8 ANALYSIS

This section is devoted to presenting our main results. First, we will discuss the setup of our fitting procedure, before discussing the results of the parameter fits.

8.1 Fitting preparation

In recent years, different areas of cosmology have been pushing for blinded analysis techniques to avoid any possible (confirmation) bias. We are using a blinded analysis with the following setup. (1) All tests of the power spectrum model, its parametrizations and possible systematic uncertainties have been done using mock catalogues only, (2) the conditions of the fit, like the maximum wavenumber, k_{\max} and the binning of the power spectrum, have been set before the data are analysed, (3) the data have been fitted only once for each fitting range.

We decided to bin the power spectrum in bins of $\Delta k = 5 \times 10^{-3} h \text{ Mpc}^{-1}$ (Percival et al. 2013) and to use the fitting range $k = 0.01\text{--}0.20 h \text{ Mpc}^{-1}$ as the main result of this paper. The choice of our maximum wavenumber, $k_{\max} = 0.20 h \text{ Mpc}^{-1}$ is based on the systematics analysis in the previous section. We will also provide the results using $k_{\max} = 0.15 h \text{ Mpc}^{-1}$ for two reasons: (1) Some people might be concerned about systematic uncertainties not considered in our analysis and (2) the results with the two different fitting ranges can be used to test the scale dependence of $f\sigma_8$, since the two cases have different effective wavenumbers. Such scale dependence is a property of many modified gravity theories. We emphasize here however, that our assumption of the scale independent $f\sigma_8$ is to some extent only a consistency check of GR. In order to constrain a modified gravity theory, it is desirable to prepare a new theoretical template in a theory-dependent manner (e.g. for $f(R)$, see Taruya et al. 2013b).

We also have to define the effective redshift of the CMASS-DR11 data set. We calculate the effective redshift by

$$z_{\text{eff}} = \frac{\sum_i^{N_{\text{gal}}} w_{\text{FKP}}(\mathbf{x}_i) z_i}{\sum_i^{N_{\text{gal}}} w_{\text{FKP}}(\mathbf{x}_i)}, \quad (67)$$

where we find $z_{\text{eff}} \approx 0.57$. This is the same effective redshift as used in the CMASS-DR9 analysis and the accompanying papers of CMASS-DR11.

Using the covariance matrix derived in Section 4 we perform a χ^2 minimization to find the best-fitting parameters. In addition to the scaling of the covariance matrix of equation (28) we have to propagate the error in the covariance matrix to the error on the

estimated parameters. We can do this by scaling the variance for each parameter by (Percival et al. 2013)

$$M = \sqrt{\frac{1 + B(n_b - n_p)}{1 + A + B(n_p + 1)}}, \quad (68)$$

where n_p is the number of parameters and

$$A = \frac{2}{(N_s - n_b - 1)(N_s - n_b - 4)}, \quad (69)$$

$$B = \frac{N_s - n_b - 2}{(N_s - n_b - 1)(N_s - n_b - 4)}. \quad (70)$$

Taking the quantities which apply in our case ($N_s = 999$, $n_b = 76$, $n_p = 7$) results in a very modest correction of $M \approx 1.03$.

8.2 Results

We are using a Markov chain Monte Carlo (MCMC) method to find the best-fitting values for the measurement of the CMASS-DR11 monopole and quadrupole. The seven free parameters of this fit are: α_{\parallel} , α_{\perp} , the growth rate $f(z_{\text{eff}})\sigma_8(z_{\text{eff}})$, the power spectrum amplitudes, $b_1\sigma_8(z_{\text{eff}})$ and $b_2\sigma_8(z_{\text{eff}})$, the velocity dispersion, σ_v and the shot noise component N .

We summarize our best-fitting results with marginalized errors for each free parameter in Table 2 and we show 2D contour plots in Figs 14 and 15. Using the fitting range $k = 0.01\text{--}0.20 h \text{ Mpc}^{-1}$ we find $\alpha_{\parallel} = 1.018 \pm 0.036$, $\alpha_{\perp} = 1.029 \pm 0.015$ and $f(z_{\text{eff}})\sigma_8(z_{\text{eff}}) = 0.419 \pm 0.042$. The constraints on α_{\parallel} and α_{\perp} can be expressed as $D_V(z_{\text{eff}})/r_s(z_d) = 13.89 \pm 0.18$ and $F_{\text{AP}} = 0.679 \pm 0.031$. Another alternative is to express the geometric constraints as the expansion rate $H(z_{\text{eff}})r_s(z_d)/r_s^{\text{fid}}(z_d) = 93.1 \pm 3.3 \text{ km s}^{-1} \text{ Mpc}^{-1}$ and the angular diameter distance $D_A(z_{\text{eff}})r_s^{\text{fid}}(z_d)/r_s(z_d) = 1388 \pm 22 \text{ Mpc}$, where $r_s(z_d)$ is the sound horizon at the drag redshift z_d . For the nuisance parameters we find $b_1\sigma_8(z_{\text{eff}}) = 1.224 \pm 0.031$, $b_2\sigma_8(z_{\text{eff}}) = -0.09 \pm 0.62$, $\sigma_v = 4.65 \pm 0.81 \text{ Mpc } h^{-1}$ and $N = 1690 \pm 600$. The χ^2 of our best fit is 140.5 with 152 bins and seven free parameters. The best-fitting χ^2 has a contribution of 66.6 from the NGC of CMASS-DR11 and 73.9 from the SGC with 76 bins each. Splitting between the monopole and quadrupole, we find that the monopole contribution to χ^2 is 79.8, while the quadrupole contribution is 68.7, again with 76 bins each.⁴ Overall we find a better fit for the NGC than for the SGC and a better fit for the quadrupole than for the monopole.

Using the fitting range $k = 0.01\text{--}0.15 h \text{ Mpc}^{-1}$ we find $\alpha_{\parallel} = 1.005 \pm 0.057$, $\alpha_{\perp} = 1.029 \pm 0.023$ and $f(z_{\text{eff}})\sigma_8(z_{\text{eff}}) = 0.423 \pm 0.052$. The constraints on α_{\parallel} and α_{\perp} can again be expressed as $D_V(z_{\text{eff}})/r_s(z_d) = 13.85 \pm 0.27$ and $F_{\text{AP}} = 0.686 \pm 0.046$ or alternatively $H(z_{\text{eff}})r_s(z_d)/r_s^{\text{fid}}(z_d) = 94.1 \pm 5.4 \text{ km s}^{-1} \text{ Mpc}^{-1}$ and $D_A(z_{\text{eff}})r_s^{\text{fid}}(z_d)/r_s(z_d) = 1389 \pm 31 \text{ Mpc}$. For the nuisance parameters we find $b_1\sigma_8(z_{\text{eff}}) = 1.222 \pm 0.044$, $b_2\sigma_8(z_{\text{eff}}) = 0.7 \pm 1.2$, $\sigma_v = 4.3 \pm 1.3 \text{ Mpc } h^{-1}$ and $N = 1080 \pm 620$. The $\chi^2/\text{d.o.f}$ of our best fit is 90.3/105.

In Fig. 14 we show the constraints on D_V/r_s , F_{AP} and $f\sigma_8$ comparing our results using the fitting range $k = 0.01\text{--}0.20 h \text{ Mpc}^{-1}$ in cyan and $k = 0.01\text{--}0.15 h \text{ Mpc}^{-1}$ in brown. While the constraints

⁴ The sum of the monopole and quadrupole contributions does not add up to the best-fitting χ^2 of 140.5, because of the cross-correlation between the monopole and quadrupole.

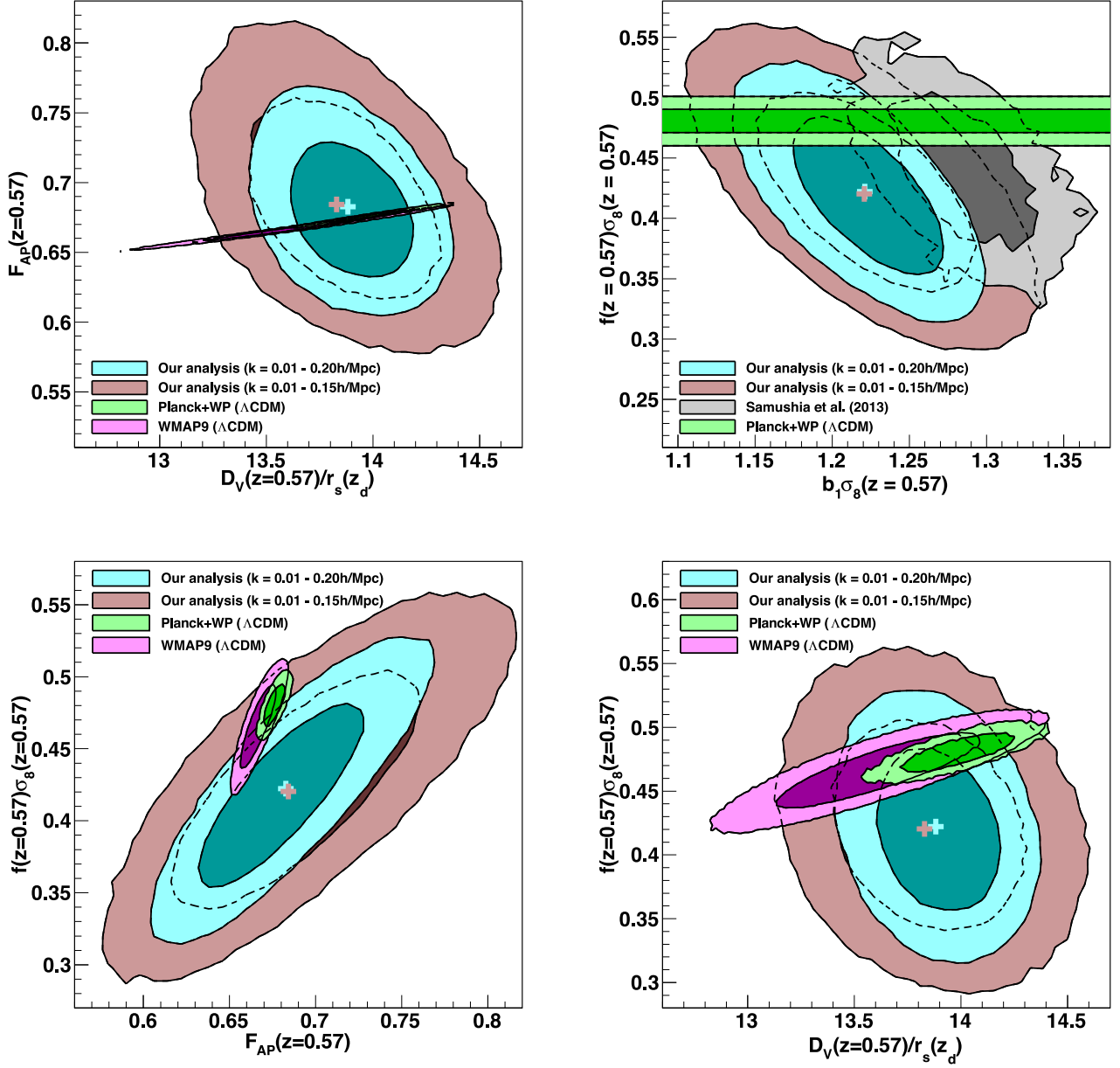


Figure 14. 2D likelihood distribution of $D_V(z_{\text{eff}})/r_s(z_d)$ and $F_{\text{AP}}(z_{\text{eff}})$ (top left), $b_1\sigma_8(z_{\text{eff}})$ and $f(z_{\text{eff}})\sigma_8(z_{\text{eff}})$ (top right), $F_{\text{AP}}(z_{\text{eff}})$ and $f(z_{\text{eff}})\sigma_8(z_{\text{eff}})$ (bottom left), $D_V(z_{\text{eff}})/r_s(z_d)$ and $f(z_{\text{eff}})\sigma_8(z_{\text{eff}})$ (bottom right). We show the 68 and 95 per cent confidence regions. The plot on the top right also includes the result of Samushia et al. (2013b). All contours are directly derived from the MCMC chains and do not include the systematic uncertainties. The crosses mark the maximum likelihood values with colours corresponding to the contours. In all plots, we also compare to Planck within Λ CDM (green contours) and WMAP9 within Λ CDM (magenta contours).

weakened for the brown contours due to the smaller number of modes, the two fits give very similar best-fitting values.

8.3 To use our results

In this subsection, we present our main results for future use, i.e. best-fitting values of the two geometric constraints ($D_V/r_s(z_d)$ and F_{AP}) and the RSD parameter together with the covariance matrix. If readers are interested in using our constraints to test cosmological models or modifications of GR, they should be aware of the assumptions underlying our constraints given in Section 6.3.

Since we present our result in a different base compared to the base we used for the study of systematics in Section 7, we made sure

that the negligible systematic uncertainties in α_{\parallel} and α_{\perp} transfer into negligible shifts in D_V/r_s and F_{AP} . For most purposes our results can be well approximated by a multivariate Gaussian likelihood with

$$V_{k_{\text{max}}=0.20}^{\text{data}} = \begin{pmatrix} D_V(z_{\text{eff}})/r_s(z_d) \\ F_{\text{AP}}(z_{\text{eff}}) \\ f(z_{\text{eff}})\sigma_8(z_{\text{eff}}) \end{pmatrix} = \begin{pmatrix} 13.88 \\ 0.683 \\ 0.422 \end{pmatrix} \quad (71)$$

and the symmetric covariance matrix is given by

$$10^3 C_{k_{\text{max}}=0.20} = \begin{pmatrix} 36.400 & -2.0636 & -1.8398 \\ & 1.0773 & 1.1755 \\ & & 1.8478 + 0.196 \end{pmatrix} \quad (72)$$

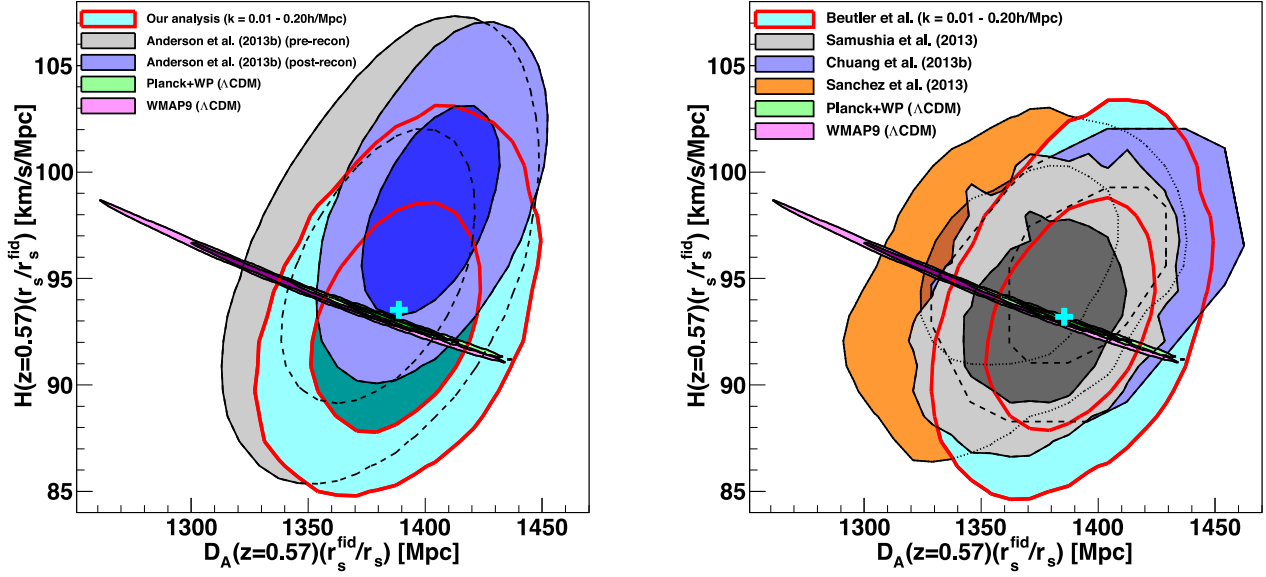


Figure 15. Comparison of the 2D likelihood distribution of $D_A(z_{\text{eff}})r_s^{\text{fid}}(z_d)/r_s(z_d)$ and $H(z_{\text{eff}})r_s(z_d)/r_s^{\text{fid}}(z_d)$. We show the 68 and 95 per cent confidence regions. The plot on the left compares our analysis (cyan contours) to the analysis by Anderson et al. (2013b) before applying density field reconstruction (grey contours) and after applying density field reconstruction (blue contours). The plot on the right compares our analysis (cyan contours) to the analysis by Samushia et al. (2013b) (grey contours), the analysis by Chuang et al. (2013b) (blue contours) and Sanchez et al. (2013) (orange contours). In both plots, we also compare to Planck within Λ CDM (green contours) and WMAP9 within Λ CDM (magenta contours).

leading to

$$C_{k_{\text{max}}=0.20}^{-1} = \begin{pmatrix} 31.032 & 77.773 & -16.796 \\ & 2687.7 & -1475.9 \\ & & 1323.0 \end{pmatrix}. \quad (73)$$

For $f\sigma_8$ we included the systematic error of 3.1 percent (see Section 7), where we assumed uncorrelated systematic errors. The sound horizon scale used in our analysis is given by $r_s(z_d) = 147.36$ Mpc. The diagonal elements of the inverse covariance matrix represent the error on the different parameters when not marginalizing over the other parameters. For example, for the growth rate we find $f(z_{\text{eff}})\sigma_8(z_{\text{eff}}) = 0.422 \pm 0.027$. Note, that this constraint assumes that we know the geometry of the Universe exactly and neglects the large correlation between $f\sigma_8$ and F_{AP} . We recommend using the full multivariate Gaussian for any cosmological model constraints.

We encourage the use of our results for $k_{\text{max}} = 0.20 h \text{ Mpc}^{-1}$, but we also provide the results using $k_{\text{max}} = 0.15 h \text{ Mpc}^{-1}$. The maximum likelihood values for the fitting range $k = 0.01\text{--}0.15 h \text{ Mpc}^{-1}$ are

$$V_{k_{\text{max}}=0.15}^{\text{data}} = \begin{pmatrix} D_V(z_{\text{eff}})/r_s(z_d) \\ F(z_{\text{eff}}) \\ f(z_{\text{eff}})\sigma_8(z_{\text{eff}}) \end{pmatrix} = \begin{pmatrix} 13.83 \\ 0.684 \\ 0.420 \end{pmatrix} \quad (74)$$

and the symmetric covariance matrix is given by

$$10^3 C_{k_{\text{max}}=0.15} = \begin{pmatrix} 84.732 & -5.7656 & -3.0985 \\ & 2.2777 & 1.9755 \\ & & 2.9532 \end{pmatrix} \quad (75)$$

leading to

$$C_{k_{\text{max}}=0.15}^{-1} = \begin{pmatrix} 14.877 & 57.455 & -22.825 \\ & 1267.7 & -787.74 \\ & & 841.62 \end{pmatrix}, \quad (76)$$

where no systematic error is included. Note that, the values above are based on the sound horizon, r_s , calculated from CAMB (Lewis, Challinor & Lasenby 2000), while the equivalent values using r_s calculated from Eisenstein & Hu (1998) are given in Appendix C. The likelihood for any cosmological model using our constraints can then be calculated as

$$\mathcal{L} \propto \exp \left[-(V^{\text{data}} - V^{\text{m}})^T C^{-1} (V^{\text{data}} - V^{\text{m}}) / 2 \right], \quad (77)$$

where V^{m} is a vector with model predictions for the three cosmological parameters.

8.4 Comparison to other measurements

In Fig. 15, we show the constraints on $H(z_{\text{eff}})r_s/r_s^{\text{fid}}$ and $D_A(z_{\text{eff}})r_s^{\text{fid}}/r_s$ from different CMASS analyses as well as the Planck prediction within Λ CDM. Our analysis using the fitting range $k = 0.01\text{--}0.20 h \text{ Mpc}^{-1}$ is included as the cyan contours. Anderson et al. (2013b) updated the CMASS-DR9 analysis published in Anderson et al. (2013a), where only the BAO information is exploited, while the RSD signal and broad-band shape is marginalized out. The BAO constraint can be improved substantially by using density field reconstruction. We compare our results with Anderson et al. (2013b) in Fig. 15 (left), before reconstruction (grey contours) and after reconstruction (blue contours). Fig. 15 (right) shows our results compared to other CMASS-DR11 studies, namely Samushia et al. (2013b) (grey contours), Chuang et al. (2013b) (blue contours) and Sanchez et al. (2013) (orange contours). While our analysis is in Fourier space, all companion BOSS-DR11 papers we compare with in Fig. 15 do their analysis in configuration space. The different CMASS-DR11 studies shown in Fig. 15 use the same data set, but use (1) different information from this data set, (2) different fitting regions and (3) different clustering models. From Fig. 15 we can see that all CMASS studies show agreement within 1σ .

In Fig. 14 (top right), we show another comparison between our result and Samushia et al. (2013b), this time using the 2D likelihood

of $f\sigma_8$ together with the power spectrum normalization, $b_1\sigma_8$. We can see that the two results agree well on $f\sigma_8$ but find different clustering amplitudes. Using the fitting range $k = 0.01\text{--}0.20 h \text{Mpc}^{-1}$ we find $b_1\sigma_8(z_{\text{eff}}) = 1.227 \pm 0.030$ while Samushia et al. (2013b) find $b_1\sigma_8(z_{\text{eff}}) = 1.289 \pm 0.032$. Using the fiducial values for $\sigma_8(z_{\text{eff}})$ the bias obtained in our analysis is $b_1 = 2.040 \pm 0.052$, while Samushia et al. (2013b) find $b_1 = 2.096 \pm 0.052$. The reason for this difference could be (1) the different scales which are used in the two different studies or (2) the details of the modelling, i.e. we include higher order bias terms: b_2, b_{s2}, b_{3nl} and N , while Samushia et al. (2013b) only include linear bias. Since the clustering amplitude is just considered a nuisance parameter in our analysis, this difference does not represent a problem for our main cosmological results. Comparing the constraints on $f\sigma_8$ with the prediction of Planck (green contours) we find that our best-fitting value is below the Planck prediction ($[f(z = 0.57)\sigma_8(z = 0.57)]_{\text{Planck}} = 0.481 \pm 0.010$) at 1.4 σ significance level, when marginalizing over all other parameters.

Reid et al. (2012) and Chuang et al. (2013a) analysed the power spectrum multipoles in CMASS-DR9 finding $f(z = 0.57)\sigma_8(z = 0.57) = 0.427^{+0.069}_{-0.063}$ (Reid et al. 2012) and $f(z = 0.57)\sigma_8(z = 0.57) = 0.428 \pm 0.066$ (Chuang et al. 2013a) in good agreement with our results. The error decreased from DR9 to DR11 by roughly a factor of 1.6, which agrees with the expectation due to the survey volume increase.

We should also mention other RSD measurements in the literature. Blake et al. (2011c) analysed the WiggleZ power spectrum simultaneously fitting for $F_{\text{AP}}(z)$ and $f(z)\sigma_8(z)$. Because of the small sky coverage of the different patches of the WiggleZ survey, it is possible to measure the power spectrum multipoles in WiggleZ using the FKP estimator (Blake et al. 2011a). They found constraints on $f(z)\sigma_8(z)$ between 21 and 32 per cent for four redshift bins (0.22, 0.41, 0.6 and 0.78). Their constraint at $z = 0.6$ is $f\sigma_8 = 0.37 \pm 0.08$, which is statistically consistent with our result. Within the luminous red galaxy sample in SDSS-II DR7, Samushia et al. (2012) reported growth of structure measurements in two redshift bins, finding $f(z = 0.25)\sigma_8(z = 0.25) = 0.351 \pm 0.058$ and $f(z = 0.37)\sigma_8(z = 0.37) = 0.460 \pm 0.038$. While Samushia et al. (2012) fixed the AP effect, Oka et al. (2013) put a simultaneous constraint on the RSD and the AP effect using the power spectrum multipoles, finding $f(z = 0.3)\sigma_8(z = 0.3) = 0.49 \pm 0.08$. The 6dFGS team recently reported a growth of structure measurement of $f(z)\sigma(z) = 0.423 \pm 0.055$ (Beutler et al. 2012) at $z = 0.067$.

We note that like the $f\sigma_8$ constraint reported in our paper, most growth of structure constraints obtained in other galaxy surveys lie below the Planck $\Lambda\text{CDM-GR}$ prediction.

9 COSMOLOGICAL IMPLICATIONS

This section contains two simple applications of the constraints we obtained with CMASS-DR11. First, we perform a ΛCDM consistency check by combining the CMASS constraints with the Planck data to test GR. The second application assumes ΛCDM and GR and constrains σ_8 using only the CMASS data set.

9.1 Consistency check using CMASS-DR11 and Planck 2013

Within $\Lambda\text{CDM-GR}$ it has been shown that the growth rate can be parametrized as $f(z) = \Omega_m^\gamma(z)$, where γ is the growth index, predicted to be $\gamma \approx 0.55$ in GR (Linder 2005). As a consistency check for $\Lambda\text{CDM-GR}$ within the Planck cosmology we use our

constraint on $f(z_{\text{eff}})\sigma_8(z_{\text{eff}})$ obtained using the fitting range $k = 0.01\text{--}0.20 h \text{Mpc}^{-1}$, to set constraints on γ . To do this, we download the Planck MCMC chain for ΛCDM^5 and importance sample this chain. The analysis method is described in the following three steps.

(i) For each MCMC chain element, we randomly choose a value of γ with the flat prior $0 < \gamma < 2$. Since the value of $\sigma_8(z_{\text{eff}})$ depends on γ we have to re-calculate this value for each chain element. First, we calculate the growth factor

$$D(a_{\text{eff}}) = \exp \left[- \int_{a_{\text{eff}}}^1 da' f(a')/a' \right], \quad (78)$$

where a_{eff} is the scalefactor at the effective redshift $a_{\text{eff}} = 1/(1 + z_{\text{eff}})$. In order to derive $\sigma_{8,\gamma}(z_{\text{eff}})$ we have to extrapolate from the matter dominated epoch to the effective redshift,

$$\sigma_{8,\gamma}(z_{\text{eff}}) = \frac{D_\gamma(z_{\text{eff}})}{D(z_{hi})} \sigma_8(z_{hi}), \quad (79)$$

where we calculate $\sigma_8(z_{hi})$ at $z_{hi} = 50$, well in the matter-dominated regime, where $f(z) \approx 1$.

(ii) Now, we calculate the growth rate using $f_\gamma(z_{\text{eff}}) \simeq \Omega_m^\gamma(z_{\text{eff}})$. This gives us all the ingredients to construct the parameter combination $f_\gamma(z_{\text{eff}})\sigma_{8,\gamma}(z_{\text{eff}})$.

(iii) We also calculate $D_V/r_s(z_d)$ and F_{AP} for each chain element. We then use the maximum likelihood values and inverse covariance matrix of equations (71) and (73) to calculate a CMASS-DR11 likelihood and combine this with the Planck likelihood.

The result is shown in Fig. 16 (left). Marginalizing over the remaining parameters we get $\gamma = 0.772^{+0.124}_{-0.097}$ (Planck+CMASS), while the prediction of $\Lambda\text{CDM+GR}$ is $\gamma \approx 0.55$. Only 1.7 per cent of the likelihood can be found below $\gamma = 0.55$ and therefore GR lies outside the 96.6 per cent confidence level. We can now ask, whether this situation changes if we use WMAP9 instead of Planck. WMAP9 measured a smaller value of Ω_m and therefore predicts a smaller value of $f\sigma_8$. If we use only the measured $f\sigma_8$, ignoring the geometric information (brown contours in Fig. 16, right) we find better agreement with $\gamma = 0.55$ compared to the same situation for Planck. When we include the geometric information (cyan contours) the errors become smaller and the preferred value of gamma changes from $\gamma = 0.65^{+0.22}_{-0.14}$ (WMAP9+ $f\sigma_8$) to $\gamma = 0.76 \pm 0.11$ (WMAP9+ $D_V/r_s, F_{\text{AP}}, f\sigma_8$), very similar to the value we find in Planck+CMASS. The shift of γ towards larger values when including geometric information is caused by the slight tension between WMAP9 and our geometric parameters. In both cases, we see that the constraints improve considerably, when including the geometric information. Since the geometric parameters are not sensitive to γ , this improvement comes through the improvement on Ω_m and σ_8 . We regard our measurement of γ using the Planck chain as the final result of this consistency check and include it in Fig. 1 at the scale of $\sim 30 \text{Mpc}$ (see Section 6.4).

From the theoretical side it is difficult to find models of modified gravity which suppress the growth of structure. Most models actually predict a stronger structure growth (see e.g. Mortonson, Hu & Huterer 2009; Dodelson & Park 2013). One example of a model which does predict smaller structure growth is the DGP model (Dvali, Gabadadze & Porrati 2000), which however has theoretical issues (Gorbinov, Koyama & Sibiryakov 2006) and also seems to predict the wrong expansion history (e.g. Davis et al. 2007; Fang et al. 2008).

⁵ http://irsa.ipac.caltech.edu/data/Planck/release_1/ancillary-data/

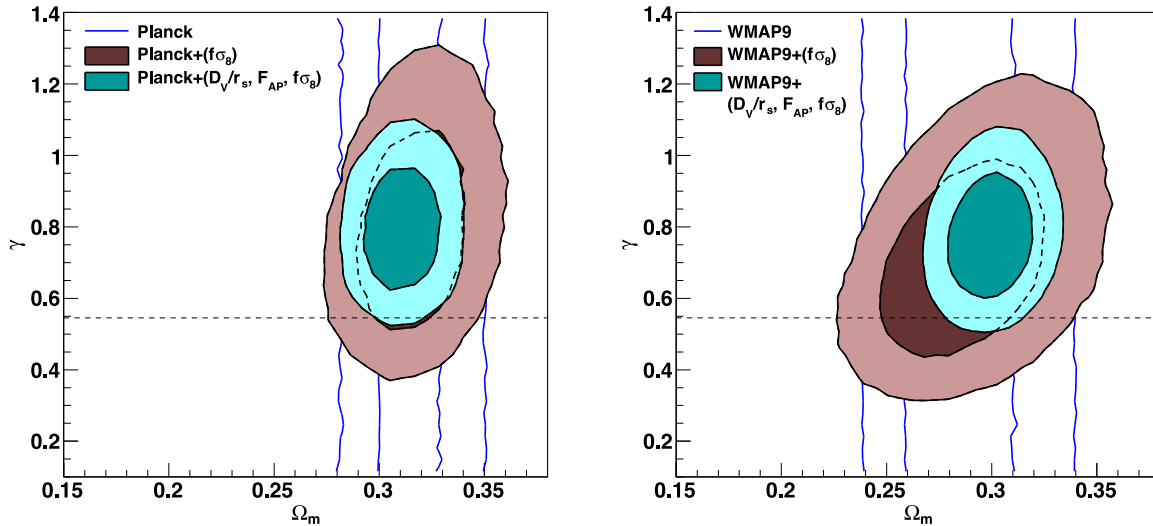


Figure 16. The 2D likelihood distribution for γ and Ω_m from Planck+CMASS (left) and WMAP9+CMASS (right). We show the 68 and 95 percent confidence regions. The different contours are for the CMB constraints alone (blue lines), CMB + $f\sigma_8$ from CMASS-DR11 (brown contours) and CMB + $(D_V/r_s, F_{AP}, f\sigma_8)$ from equations (71) and (73) (cyan contours). Since we do not exploit the integrated Sachs-Wolfe effect for this test, the CMB data sets cannot set constraints on γ . The CMB data are needed for tight constraints on Ω_m and for the normalization of the power spectrum, $\sigma_8(z)$.

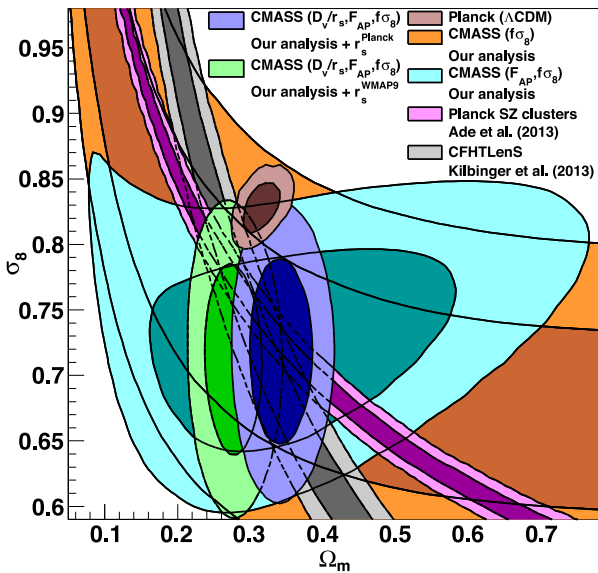


Figure 17. Comparison between Planck (Ade et al. 2013a), Planck SZ clusters (Ade et al. 2013b), CFHTLenS lensing (Kilbinger et al. 2013) and our results in the σ_8 – Ω_m plane. When using only the $f\sigma_8$ constraint from our analysis (orange contours), there is a degeneracy, similar to the cluster and lensing data sets. The geometric information can break this degeneracy. While the AP effect is only depending on Ω_m , our D_V/r_s constraint does require calibration of the sound horizon. We show the results, where we fix the sound horizon to the value of Planck (blue contours) and the value reported by WMAP9 (green contours). The results are summarized in Table 3. To turn our $f\sigma_8$ constraint into a constraint on σ_8 we assume GR ($\gamma = 0.55$) and Λ CDM similar to the Planck contours (brown contours). The tension in σ_8 between our measurement and Planck is directly related to the large γ we find in our Λ CDM consistency check in Section 9.1.

There are many ways in which one could reduce the predicted structure growth of Planck, e.g. massive neutrinos, $w < -1$ or $\Omega_k > 0$. We should also mention that there are several other data sets in tension with the Planck inferred structure growth. Fig. 17 shows our result in the σ_8 – Ω_m plane compared to Planck (Ade et al.

2013a), Planck SZ clusters (Ade et al. 2013b) and CHFTLS lensing (Kilbinger et al. 2013). Using the CMASS $f\sigma_8$ measurement alone, there is a degeneracy between σ_8 and Ω_m similar to the lensing and cluster constraints. This degeneracy can be broken when including the geometric information (F_{AP} and D_V/r_s). We can see that Planck predicts a large σ_8 in tension with the other data sets included in this comparison (see also Mandelbaum et al. 2013). The large normalization σ_8 of Planck directly leads to the large γ we found in our consistency check above. Therefore, Fig. 17 shows that we can relax the tension between our measurement and GR by using the normalization from one of the other data sets shown in this figure.

9.2 Constraining σ_8 with CMASS-DR11

Assuming Λ CDM and GR in the form $\Omega_m^{0.55}(z)$, we can use our constraint on the growth of structure ($f\sigma_8$) and the AP effect (F_{AP}) to set the constraint $\sigma_8 = 0.731 \pm 0.052$ (cyan contours in Fig. 17). Our data set is therefore one of the few low-redshift data sets, which is powerful enough to constrain σ_8 independently. We can also get a fairly weak constraint on the matter density of $\Omega_m = 0.33^{+0.15}_{-0.12}$.

Additionally, we can include the BAO information (D_V/r_s), where we however have to fix the sound horizon size r_s . In Fig. 17, we show the constraint using the sound horizon of Planck (blue contours) and WMAP9 (green contours). We use the sound horizon in comoving units $r_s^{\text{Planck}}(z_d) = 98.79 \text{ Mpc } h^{-1}$ and $r_s^{\text{WMAP9}}(z_d) = 102.06 \text{ Mpc } h^{-1}$, which includes information about the Hubble constant. Our constraint on D_V/r_s together with the sound horizon from the CMB allows tight constraints on Ω_m , while the constraint on σ_8 does not improve significantly (see Table 3 for details).

10 CONCLUSION

This paper analyses the BOSS CMASS-DR11 data set employing a power spectrum estimator suggested by Yamamoto et al. (2006), which allows us to measure the power spectrum monopole and quadrupole in a wide-angle survey like BOSS. We use QPM simulations to produce 999 mock catalogues to derive a covariance matrix. The covariance matrix shows little correlation between the

Table 3. This table summarizes cosmological parameter constraints obtained in Section 9 using CMASS-DR11. The first four rows contain constraints on the growth index γ and Ω_m when combining CMASS with Planck and *WMAP9* (see Fig. 16). The fifth and sixth rows contain constraints on σ_8 and Ω_m using only the growth rate and the AP effect ($f\sigma_8$ and F_{AP}) of the CMASS data set. The last four rows contain constraints on σ_8 and Ω_m using all CMASS-DR11 constraints (D_V/r_s , F_{AP} and $f\sigma_8$) and assuming the sound horizon of Planck or *WMAP9* (see Fig. 17) in comoving units. In this case the constraint on Ω_m is dependent on the CMB experiment used to calibrate the standard ruler, while the constraint on σ_8 is fairly independent of this choice.

Parameter constraint	Based on	Assumptions	
Section 9.1			
γ	$0.772^{+0.124}_{-0.097}$	CMASS- $(D_V/r_s, F_{AP}, f\sigma_8)$ + Planck	Λ CDM, $\Omega_m^\gamma(z)$
Ω_m	0.308 ± 0.011	CMASS- $(D_V/r_s, F_{AP}, f\sigma_8)$ + Planck	Λ CDM, $\Omega_m^\gamma(z)$
γ	0.76 ± 0.11	CMASS- $(D_V/r_s, F_{AP}, f\sigma_8)$ + <i>WMAP9</i>	Λ CDM, $\Omega_m^\gamma(z)$
Ω_m	0.298 ± 0.013	CMASS- $(D_V/r_s, F_{AP}, f\sigma_8)$ + <i>WMAP9</i>	Λ CDM, $\Omega_m^\gamma(z)$
Section 9.2			
σ_8	0.731 ± 0.052	CMASS- $(F_{AP}, f\sigma_8)$	Λ CDM, $\Omega_m^{0.55}(z)$
Ω_m	$0.33^{+0.15}_{-0.12}$	CMASS- $(F_{AP}, f\sigma_8)$	Λ CDM, $\Omega_m^{0.55}(z)$
σ_8	0.719 ± 0.047	CMASS- $(D_V/r_s, F_{AP}, f\sigma_8)$	Λ CDM, $\Omega_m^{0.55}(z)$, $r_s^{\text{Planck}}(z_d) = 98.79 \text{ Mpc } h^{-1}$
Ω_m	0.341 ± 0.028	CMASS- $(D_V/r_s, F_{AP}, f\sigma_8)$	Λ CDM, $\Omega_m^{0.55}(z)$, $r_s^{\text{Planck}}(z_d) = 98.79 \text{ Mpc } h^{-1}$
σ_8	0.713 ± 0.047	CMASS- $(D_V/r_s, F_{AP}, f\sigma_8)$	Λ CDM, $\Omega_m^{0.55}(z)$, $r_s^{\text{WMAP9}}(z_d) = 102.06 \text{ Mpc } h^{-1}$
Ω_m	0.274 ± 0.023	CMASS- $(D_V/r_s, F_{AP}, f\sigma_8)$	Λ CDM, $\Omega_m^{0.55}(z)$, $r_s^{\text{WMAP9}}(z_d) = 102.06 \text{ Mpc } h^{-1}$

different bins in the power spectrum, which is very different to similar studies using the correlation function.

Our model of the multipole power spectrum accounts for non-linear evolution on the basis of PT. We adopt the modelling of non-linear RSD by Taruya et al. (2010) and extend this approach to include the local and non-local galaxy bias with its stochasticity.

The parameter fits using the fitting range $k = 0.01\text{--}0.20 \text{ h Mpc}^{-1}$ are considered the main results of this paper. We provide a multivariate Gaussian likelihood to use our results for cosmological constraints.

Our analysis has been performed blind, meaning that all systematics checks and the set-up of the fitting procedure has been done on mock catalogues and only at the last stage did we analyse the actual CMASS-DR11 power spectrum measurement. The results of our analysis can be summarized in the following five points.

(i) We provide a set of equations (equations 32, 33, 36, 37), which allows us to incorporate the window function and the integral constraint into our analysis in a self-consistent manner, without using any simplifying assumptions and without the need to split the survey into subregions.

(ii) Our study of systematic uncertainties lead to a maximum wavenumber of $k_{\text{max}} = 0.20 \text{ h Mpc}^{-1}$ for our analysis, where the total error of $f(z_{\text{eff}})\sigma_8(z_{\text{eff}})$ is minimized. Our final systematic uncertainty for $f(z_{\text{eff}})\sigma_8(z_{\text{eff}})$ is 3.1 percent when using the fitting range $k = 0.01\text{--}0.20 \text{ h Mpc}^{-1}$. The geometric parameters α_{\parallel} and α_{\perp} (D_V/r_s and F_{AP}) do not show any significant systematic uncertainties.

(iii) Our power spectrum model includes seven free parameters: the two geometric parameters, α_{\parallel} and α_{\perp} , the growth rate $f(z_{\text{eff}})\sigma_8(z_{\text{eff}})$ and four nuisance parameters. We find $\alpha_{\parallel} = 1.018 \pm 0.036$, $\alpha_{\perp} = 1.029 \pm 0.015$ and $f(z_{\text{eff}})\sigma_8(z_{\text{eff}}) = 0.419 \pm 0.044$, where we included the systematic uncertainty of 3.1 percent. The geometric parameters α_{\parallel} and α_{\perp} can be expressed as $D_V(z_{\text{eff}})/r_s(z_d) = 13.89 \pm 0.18$ and $F_{AP}(z_{\text{eff}}) = (1 + z_{\text{eff}})D_A(z_{\text{eff}})H(z_{\text{eff}})/c = 0.679 \pm 0.031$. While the geometric parameters found in our analysis agree very well with the Planck prediction within Λ CDM, the growth rate is about 1.4σ below the Planck prediction. We provide a multivariate Gaussian likelihood to use our results (see Section 8.3). All results are summarized

in Table 2, where we also provide the parameter constraints using the more conservative fitting range $k = 0.01\text{--}0.15 \text{ h Mpc}^{-1}$. We also provide the power spectrum measurements itself, together with the covariance matrices and the window functions online at https://sdss3.org/science/boss_publications.php.

(iv) We performed a Λ CDM–GR consistency check within the Planck cosmology, which results in a measurement of the growth index $\gamma = 0.772^{+0.124}_{-0.097}$. This value excludes the GR prediction of $\gamma \approx 0.55$ by more than 2σ . When replacing Planck with *WMAP9* we find a very similar result of $\gamma = 0.76 \pm 0.11$. We conclude that there is tension between our result combined with Planck (*WMAP9*) and the prediction by GR. This tension could be (1) a statistical fluctuation, (2) an indication for unaccounted systematic uncertainties in CMASS and/or Planck (*WMAP9*) or (3) ask for modifications in Λ CDM or GR.

(v) Assuming Λ CDM and GR we can use our measurement of the growth rate ($f\sigma_8$) together with the information from the AP effect (F_{AP}) to constrain $\sigma_8 = 0.731 \pm 0.052$. The low value of σ_8 is directly connected to the high value of the growth index γ obtained from our data set. While galaxy data sets in the past only constrained a degenerate combination of σ_8 and Ω_m , our data is now good enough to break this degeneracy. This represents one of the best independent σ_8 constraints at low redshift.

Finally, we should also mention that separate studies within the BOSS collaboration are currently working on measurements of CMASS clustering combined with lensing, as well as measurements of the CMASS bispectrum, which should provide additional information about the bias parameters b_1 and b_2 , respectively. This will help us to go from $f\sigma_8$ directly to the growth rate f and test gravity models without using the CMB normalization.

ACKNOWLEDGEMENTS

FB would like to thank Chris Blake, Uros Seljak, Eric Linder, Beth Reid, Martin White, Morag Scrimgeour and Julien Guy for helpful discussion. SS is supported by a Grant-in-Aid for Young Scientists (Start-up) from the Japan Society for the Promotion of Science (JSPS) (no. 25887012).

Funding for SDSS-III has been provided by the Alfred P. Sloan Foundation, the Participating Institutions, the National Science Foundation, and the U.S. Department of Energy Office of Science. The SDSS-III web site is <http://www.sdss3.org/>.

SDSS-III is managed by the Astrophysical Research Consortium for the Participating Institutions of the SDSS-III Collaboration including the University of Arizona, the Brazilian Participation Group, Brookhaven National Laboratory, Carnegie Mellon University, University of Florida, the French Participation Group, the German Participation Group, Harvard University, the Instituto de Astrofísica de Canarias, the Michigan State/Notre Dame/JINA Participation Group, Johns Hopkins University, Lawrence Berkeley National Laboratory, Max Planck Institute for Astrophysics, Max Planck Institute for Extraterrestrial Physics, New Mexico State University, New York University, Ohio State University, Pennsylvania State University, University of Portsmouth, Princeton University, the Spanish Participation Group, University of Tokyo, University of Utah, Vanderbilt University, University of Virginia, University of Washington, and Yale University.

This research used resources of the National Energy Research Scientific Computing Center, which is supported by the Office of Science of the U.S. Department of Energy under Contract no. DE-AC02-05CH11231.

REFERENCES

- Ade P. A. R. et al. (Planck Collaboration), 2013a, [arXiv:1303.5076](https://arxiv.org/abs/1303.5076)
Ade P. A. R. et al. (Planck Collaboration), 2013b, [arXiv:1303.5080](https://arxiv.org/abs/1303.5080)
Anderson L. et al., 2012, *MNRAS*, 427, 3435
Anderson L. et al., 2013a, *MNRAS*, 439, 83
Anderson L. et al., 2013b, *MNRAS*, 441, 24
Alcock C., Paczynski B., 1979, *Nature*, 281, 358
Baldauf T., Seljak U., Desjacques V., McDonald P., 2012, *Phys. Rev. D*, 86, 083540
Baldauf T., Seljak U., Smith R. E., Hamaus N., Desjacques V., 2013, *Phys. Rev. D*, 88, 083507
Ballinger W. E., Peacock J. A., Heavens A. F., 1996, *MNRAS*, 282, 877
Bardeen J. M., Bond J. R., Kaiser N., Szalay A. S., 1986, *ApJ*, 304, 15
Baugh C. M., Efstathiou G., 1993, *MNRAS*, 265, 145B
Beutler F. et al., 2011, *MNRAS*, 416, 3017
Beutler F. et al., 2012, *MNRAS*, 423, 3430
Blake C. et al., 2011a, *MNRAS*, 415, 2876
Blake C. et al., 2011b, *MNRAS*, 418, 1707
Blake C. et al., 2011c, *MNRAS*, 418, 1725
Blazek J., Seljak U., Vlah Z., Okumura T., 2013, *J. Cosmol. Astropart. Phys.*, 04, 001
Bolton A. S. et al. (Cutler Group LP Collaboration), 2012, *AJ*, 144, 144
Capozziello S., De Laurentis M., 2013, [arXiv:1307.4523](https://arxiv.org/abs/1307.4523)
Carlson J., White M., Padmanabhan N., 2009, *Phys. Rev. D*, 80, 043531
Casas-Miranda R., Mo H. J., Sheth R. K., Boerner G., 2002, *MNRAS*, 333, 730
Chan K. C., Scoccimarro R., Sheth R. K., 2012, *Phys. Rev. D*, 85, 083509
Chuang C.-H. et al., 2013a, *MNRAS*, 433, 3559
Chuang C.-H. et al., 2013b, [arXiv:1312.4889](https://arxiv.org/abs/1312.4889)
Clifton T., Ferreira P. G., Padilla A., Skordis C., 2012, *Phys. Rep.*, 513, 1
Cole S. et al. (2dFGRS Collaboration), 2005, *MNRAS*, 362, 505
Crocce M., Scoccimarro R., 2006, *Phys. Rev. D*, 73, 063520
Davis T. M. et al., 2007, *ApJ*, 666, 716
Dawson K. S. et al. (BOSS Collaboration), 2013, *AJ*, 145, 10
Dekel A., Lahav O., 1999, *ApJ*, 520, 24
de la Torre S., Guzzo L., 2012, *MNRAS*, 427, 327
de Laix A. A., Starkman G., 1997, *ApJ*, 501, 427
Desjacques V., Sheth R. K., 2010, *Phys. Rev. D*, 81, 023526
Dodelson S., Park S., 2013, [arXiv:1310.4329](https://arxiv.org/abs/1310.4329)
Doi M. et al., 2010, *AJ*, 139, 1628
Dvali G. R., Gabadadze G., Porrati M., 2000, *Phys. Lett. B*, 485, 208
Eisenstein D. J., Hu W., 1998, *ApJ*, 496, 605
Eisenstein D. J., White M. J., 2004, *Phys. Rev. D*, 70, 103523
Eisenstein D. J. et al. (SDSS Collaboration), 2005, *ApJ*, 633, 560
Eisenstein D. J. et al. (SDSS Collaboration), 2011, *AJ*, 142, 72
Fang W., Wang S., Hu W., Haiman Z., Hui L., May M., 2008, *Phys. Rev. D*, 78, 103509
Feldman H. A., Kaiser N., Peacock J. A., 1994, *ApJ*, 426, 23
Freeman K. C., 1970, *ApJ*, 160, 811
Fukugita M., Ichikawa T., Gunn J. E., Doi M., Shimasaku K., Schneider D. P., 1996, *AJ*, 111, 1748
Gorbunov D., Koyama K., Sibiryakov S., 2006, *Phys. Rev. D*, 73, 044016
Gunn J. E. et al. (SDSS Collaboration), 1998, *AJ*, 116, 3040
Gunn J. E. et al. (SDSS Collaboration), 2006, *AJ*, 131, 2332
Guo H., Zehavi I., Zheng Z., 2012, *ApJ*, 756, 127
Guzzo L. et al., 2008, *Nature*, 451, 541
Hemant M. D. P., Wang Y., Chuang C.-H., 2013, [arXiv:1310.6468](https://arxiv.org/abs/1310.6468)
Hamaus N., Seljak U., Desjacques V., Smith R. E., Baldauf T., 2010, *Phys. Rev. D*, 82, 043515
Hamilton A. J. S., 1998, *The Evolving Universe*. Kluwer, Dordrecht
Hartlap J., Simon P., Schneider P., 2007, *A&A*, 464, 399
Hawkins E. et al., 2003, *MNRAS*, 346, 78
Hikage C., Yamamoto K., 2013, *J. Cosmol. Astropart. Phys.*, 1308, 019
Hikage C., Takada M., Spergel D. N., 2012a, *MNRAS*, 419, 3457
Hikage C., Mandelbaum R., Takada M., Spergel D. N., 2012b, *MNRAS*, 435, 2345
Hulse R. A., Taylor J. H., 1975, *ApJ*, 195, L51
Ishikawa T., Totani T., Nishimichi T., Takahashi R., Yoshida N., Tonegawa M., 2013, [arXiv:1308.6087](https://arxiv.org/abs/1308.6087)
Jain B., Khoury J., 2010, *Ann. Phys.*, 325, 1479
Kahn F. D., Woltjer L., 1959, *ApJ*, 130, 705
Kaiser N., 1987, *MNRAS*, 227, 1
Kilbinger M. et al., 2013, *MNRAS*, 430, 2200
Lewis A., Challinor A., Lasenby A., 2000, *ApJ*, 538, 473
Lin H., Kirshner R. P., Shectman S. A., Landy S. D., Oemler A., Tucker D. L., Schechter P. L., 1996, *ApJ*, 471, 617
Linder E. V., 2005, *Phys. Rev. D*, 72, 043529
Manera M., Gaztanaga E., 2011, *MNRAS*, 415, 383
Manera M. et al., 2012, *MNRAS*, 428, 1036
Masaki S., Hikage C., Takada M., Spergel D. N., Sugiyama N., 2013, *MNRAS*, 433, 3506
Matsubara T., 2008a, *Phys. Rev. D*, 77, 063530
Matsubara T., 2008b, *Phys. Rev. D*, 78, 083519 [erratum: *ibid*, D, 78, 109901]
Matsubara T., 2011, *Phys. Rev. D*, 83, 083518
Matsubara T., 2013, [arXiv:1304.4226](https://arxiv.org/abs/1304.4226)
Matsubara T., Suto Y., 1996, *ApJ*, 470, L1
McDonald P., Roy A., 2009, *J. Cosmol. Astropart. Phys.*, 0908, 020
Mehta K. T., Seo H. -J., Eckel J., Eisenstein D. J., Metchnik M., Pinto P., Xu X., 2011, *ApJ*, 734, 94
Mortonson M. J., Hu W., Huterer D., 2009, *Phys. Rev. D*, 79, 023004
Nishimichi T., Oka A., 2013, [arXiv:1310.2672](https://arxiv.org/abs/1310.2672)
Nishimichi T., Taruya A., 2011, *Phys. Rev. D*, 84, 043526
Mandelbaum R., Slosar A., Baldauf T., Seljak U., Hirata C. M., Nakajima R., Reyes R., Smith R. E., 2013, *MNRAS*, 432, 1544
Miyatake H. et al., 2013, [arXiv:1311.1480](https://arxiv.org/abs/1311.1480)
Oka A., Saito S., Nishimichi T., Taruya A., Yamamoto K., 2013, *MNRAS*, 439, 2515
Padmanabhan N., White M., 2009, *Phys. Rev. D*, 80, 063508
Padmanabhan N., Xu X., Eisenstein D. J., Scalzo R., Cuesta A. J., Mehta K. T., Kazin E., 2012, *MNRAS*, 427, 2132
Papai P., Szapudi I., 2008, *MNRAS*, 389, 292
Peacock J. A., Nicholson J. A., 1991, *MNRAS*, 253, 307
Peacock J. A. et al., 2001, *Nature*, 410, 169
Percival W. J. et al. (2dFGRS Collaboration), 2001, *MNRAS*, 327, 1297
Percival W. J. et al., 2007, *ApJ*, 657, 645
Percival W. J. et al., 2013, *MNRAS*, 439, 2531

Perlmutter S. et al. (Supernova Cosmology Project Collaboration), 1999, ApJ, 517, 565
 Pound R. V., Rebka G. A., Jr, 1960, Phys. Rev. Lett., 4, 337
 Rapetti D., Blake C., Allen S. W., Mantz A., Parkinson D., Beutler F., 2012, MNRAS, 432, 973
 Reid B. A., White M., 2011, MNRAS, 417, 1913
 Reid B. A. et al., 2012, MNRAS, 426, 2719
 Reid B. A., Seo H.-J., Leauthaud A., Tinker J. L., White M., 2014, preprint (arXiv:1404.3742)
 Riess A. G. et al. (Supernova Search Team Collaboration), 1998, AJ, 116, 1009
 Ross A. J. et al. (BOSS Collaboration), 2012a, MNRAS, 424, 564
 Ross A. J. et al. (BOSS Collaboration), 2012b, MNRAS, 428, 1116
 Rubin V. C., Ford W. K., Jr, 1970, ApJ, 159, 379
 Saito S., Baldauf T., Vlah Z., Seljak U., Okumura T., McDonald P., 2014, arXiv:1405.1447
 Samushia L., Percival W. J., Raccanelli A., 2012, MNRAS, 420, 2102
 Samushia L. et al., 2013a, MNRAS, 429, 1514
 Samushia L. et al., 2013b, MNRAS, 439, 3504
 Sanchez A. G. et al., 2013, MNRAS, 440, 2692
 Sato T., Huetsi G., Yamamoto K., 2011, Prog. Theor. Phys., 125, 187
 Sato T., Htsi G., Nakamura G., Yamamoto K., 2013, Int. J. Astron. Astrophys., 3, 243
 Schlegel D. et al. (SDSS-III Collaboration), 2009, Science White Papers, 314
 Scoccimarro R., 2004, Phys. Rev. D, 70, 083007
 Seljak U., McDonald P., 2011, J. Cosmol. Astropart. Phys., 1111, 039
 Seljak U., Hamaus N., Desjacques V., 2009, Phys. Rev. Lett., 103, 091303
 Sargent W. L. W., Turner E. L., 1977, ApJ, 212, 3
 Slosar A. et al., 2013, J. Cosmol. Astropart. Phys., 1304, 026
 Smee S. et al., 2013, AJ, 146, 32
 Smith J. A. et al. (SDSS Collaboration), 2002, AJ, 123, 2121
 Taruya A., Hiramatsu T., 2008, ApJ, 674, 617
 Taruya A., Nishimichi T., Saito S., Hiramatsu T., 2009, Phys. Rev. D, 80, 123503
 Taruya A., Nishimichi T., Saito S., 2010, Phys. Rev. D, 82, 063522
 Taruya A., Bernardeau F., Nishimichi T., Codis S., 2012, Phys. Rev. D, 86, 103528
 Taruya A., Nishimichi T., Bernardeau F., 2013a, Phys. Rev. D, 87, 083509
 Taruya A., Koyama K., Hiramatsu T., Oka A., 2013b, Phys. Rev. D, 89, 043509
 Tegmark M. et al. (SDSS Collaboration), 2006, Phys. Rev. D, 74, 123507
 Tinker J. L. et al., 2012, ApJ, 745, 16
 Vessot R. F. C. et al., 1980, Phys. Rev. Lett., 45, 2081
 Vlah Z., Seljak U., Okumura T., Desjacques V., 2012a, J. Cosmol. Astropart. Phys., 10, 053
 Vlah Z., Seljak U., McDonald P., Okumura T., Baldauf T., 2012b, J. Cosmol. Astropart. Phys., 1211, 009
 Wang L., Reid B., White M., 2013, MNRAS, 437, 588
 White M. et al., 2011, ApJ, 728, 126
 White M., Tinker J. L., McBride C., 2013, MNRAS, 437, 2594
 Will C. M., 2006, Living Rev. Relativ., 9, 3
 Yamamoto K., Nakamichi M., Kamino A., Bassett B. A., Nishioka H., 2006, PASJ, 58, 93
 Yamamoto K., Sato T., Huetsi G., 2008, Prog. Theor. Phys., 120, 609
 Yoo J., Seljak U., 2013, arXiv:1308.1093
 Zwicky F., 1937, ApJ, 86, 217

APPENDIX A: DERIVATION OF THE MINIMUM VARIANCE WEIGHT, w_{FKP} IN THE PRESENCE OF SYSTEMATIC WEIGHTS

This derivation follows the original derivation in Feldman et al. (1994), with the addition of a systematic weight, w_{sys} . Under the assumption that the width Δk of the spherical shell (or bin size) is larger than the coherence length ($\sim 1/D$, with D being the size of

the survey) we can write the error in the power spectrum as

$$\sigma_P^2(k) \simeq \frac{1}{V_k} \int d\mathbf{k}' |P(\mathbf{k})Q(\mathbf{k}') + S(\mathbf{k}')|^2 \quad (\text{A.1})$$

with

$$Q(\mathbf{k}) = \frac{1}{A} \int d\mathbf{x} n_g'^2(\mathbf{x}) w_{\text{FKP}}^2(\mathbf{x}) e^{-i\mathbf{k}\cdot\mathbf{x}} \quad (\text{A.2})$$

$$S(\mathbf{k}) = \frac{1}{A} \left(\int d\mathbf{x} n_g'(\mathbf{x}) w_{\text{sys}}(\mathbf{x}) w_{\text{FKP}}^2(\mathbf{x}) e^{-i\mathbf{k}\cdot\mathbf{x}} + \alpha \int d\mathbf{x} n_g'(\mathbf{x}) w_{\text{FKP}}^2(\mathbf{x}) e^{-i\mathbf{k}\cdot\mathbf{x}} \right) \quad (\text{A.3})$$

and the normalization $A = \int d\mathbf{x} n_g'^2(\mathbf{x}) w_{\text{FKP}}^2(\mathbf{x})$. The fractional variance of the power can be written as

$$\left(\frac{\sigma_P(k)}{P(k)} \right)^2 = \frac{1}{V_k} \int d\mathbf{k}' \left| Q(\mathbf{k}') + \frac{S(\mathbf{k}')}{P(\mathbf{k})} \right|^2 \quad (\text{A.4})$$

$$= \frac{1}{V_k A^2} \int d\mathbf{k}' \left| \int d\mathbf{x} w_{\text{FKP}}^2(\mathbf{x}) e^{-i\mathbf{k}'\cdot\mathbf{x}} \left(n_g'^2(\mathbf{x}) + \frac{n_g'(\mathbf{x}) w_{\text{sys}}(\mathbf{x}) + \alpha n_g'(\mathbf{x})}{P(\mathbf{k})} \right) \right|^2. \quad (\text{A.5})$$

Using Parseval's theorem in the form

$$\int d\mathbf{k}' \left| \int d\mathbf{x} F(\mathbf{x}) e^{-i\mathbf{k}'\cdot\mathbf{x}} \right|^2 = (2\pi)^3 \int d\mathbf{x} F^2(\mathbf{x}) \quad (\text{A.6})$$

the equation can be further simplified to

$$\left(\frac{\sigma_P(k)}{P(k)} \right)^2 = \frac{(2\pi)^3}{V_k A^2} \int d\mathbf{x} w_{\text{FKP}}^4(\mathbf{x}) \times \left(n_g'^2(\mathbf{x}) + \frac{n_g'(\mathbf{x}) w_{\text{sys}}(\mathbf{x}) + \alpha n_g'(\mathbf{x})}{P(\mathbf{k})} \right)^2. \quad (\text{A.7})$$

Introducing the functions

$$f(\mathbf{x}) = \left(n_g'^2(\mathbf{x}) + \frac{n_g'(\mathbf{x}) w_{\text{sys}}(\mathbf{x}) + \alpha n_g'(\mathbf{x})}{P(\mathbf{k})} \right)^2, \quad (\text{A.8})$$

$$g(\mathbf{x}) = n_g'^2(\mathbf{x}) \quad (\text{A.9})$$

we can write

$$\left(\frac{\sigma_P(k)}{P(k)} \right)^2 = \frac{\int d\mathbf{x} w_{\text{FKP}}^4(\mathbf{x}) f(\mathbf{x})}{\left[\int d\mathbf{x} w_{\text{FKP}}^2(\mathbf{x}) g(\mathbf{x}) \right]^2}. \quad (\text{A.10})$$

Now we perturb the weight $w_{\text{FKP}}(\mathbf{x}) \rightarrow w_{\text{FKP}}(\mathbf{x}) + \Delta w(\mathbf{x})$, which leads to

$$\left(\frac{\sigma_P(k)}{P(k)} \right)^2 = \frac{\int d\mathbf{x} [w_{\text{FKP}}(\mathbf{x}) + \Delta w(\mathbf{x})]^4 f(\mathbf{x})}{\left(\int d\mathbf{x} [w_{\text{FKP}}(\mathbf{x}) + \Delta w(\mathbf{x})]^2 g(\mathbf{x}) \right)^2} \quad (\text{A.11})$$

$$\simeq \frac{\int d\mathbf{x} w_{\text{FKP}}^4(\mathbf{x}) \left[1 + 4 \frac{\Delta w(\mathbf{x})}{w_{\text{FKP}}(\mathbf{x})} \right] f(\mathbf{x})}{\left[\int d\mathbf{x} w_{\text{FKP}}^2(\mathbf{x}) \left[1 + 2 \frac{\Delta w(\mathbf{x})}{w_{\text{FKP}}(\mathbf{x}_i)} \right] g(\mathbf{x}) \right]^2}. \quad (\text{A.12})$$

Using Taylor expansion up to 2nd order around $\Delta w = 0$ we get

$$\begin{aligned} \left(\frac{\sigma_P(k)}{P(k)}\right)^2 &= \frac{\int d^3x w_{\text{FKP}}^4(\mathbf{x})f(\mathbf{x})}{\left[\int d^3x w_{\text{FKP}}^2(\mathbf{x})g(\mathbf{x})\right]^2} \\ &\times \left(1 + 4 \left[\frac{\int d^3x w_{\text{FKP}}^3(\mathbf{x})f(\mathbf{x})\Delta w(\mathbf{x})}{\int d^3x w_{\text{FKP}}^4(\mathbf{x})f(\mathbf{x})} \right. \right. \\ &\left. \left. - \frac{\int d^3x w_{\text{FKP}}(\mathbf{x})g(\mathbf{x})\Delta w(\mathbf{x})}{\int d^3x w_{\text{FKP}}^2(\mathbf{x})g(\mathbf{x})} \right] \right) + \dots \end{aligned} \quad (\text{A.13})$$

Therefore, the optimal weighting function has to satisfy

$$\frac{\int d^3x w_{\text{FKP}}^3(\mathbf{x})f(\mathbf{x})\Delta w(\mathbf{x})}{\int d^3x w_{\text{FKP}}^4(\mathbf{x})f(\mathbf{x})} = \frac{\int d^3x w_{\text{FKP}}(\mathbf{x})g(\mathbf{x})\Delta w(\mathbf{x})}{\int d^3x w_{\text{FKP}}^2(\mathbf{x})g(\mathbf{x})}. \quad (\text{A.14})$$

The solution of this equation is given by

$$w_{\text{FKP}}(\mathbf{x}) \propto \sqrt{\frac{g(\mathbf{x})}{f(\mathbf{x})}} = \frac{n'(\mathbf{x})}{n'^2(\mathbf{x}) + \frac{n'_g(\mathbf{x})w_{\text{sys}}(\mathbf{x}) + \alpha n'_g(\mathbf{x})}{P(k)}} \quad (\text{A.15})$$

$$= \frac{1}{n'(\mathbf{x}) + \frac{w_{\text{sys}}(\mathbf{x}) + \alpha}{P(k)}}. \quad (\text{A.16})$$

Finally, the dimensionless optimal weighting function is

$$w_{\text{FKP}}(\mathbf{x}) = \frac{1}{\frac{P(k)n'(\mathbf{x})}{w_{\text{sys}}(\mathbf{x})} + 1 + \frac{\alpha}{w_{\text{sys}}(\mathbf{x})}}. \quad (\text{A.17})$$

When we choose a large number of random galaxies ($\alpha \ll 1$), we get

$$w_{\text{FKP}}(\mathbf{x}) = \frac{1}{1 + \frac{P(k)n'(\mathbf{x})}{w_{\text{sys}}(\mathbf{x})}}. \quad (\text{A.18})$$

which in the case of $w_{\text{sys}} = 1$ recovers the original minimum variance weight reported in Feldman et al. (1994).

APPENDIX B: WINDOW FUNCTION

B1 The survey window function: derivation of equation (33)

We simplify the convolution integral of equation (32) to

$$\begin{aligned} P_\ell^{\text{conv}}(k) &= \frac{2\ell + 1}{2} \int d\mu \int \frac{d\phi}{2\pi} \int d\mathbf{k}' P^{\text{true}}(\mathbf{k}') |W(\mathbf{k} - \mathbf{k}')|^2 \mathcal{L}_\ell(\mu) \\ &= \frac{2\ell + 1}{2} \int d\mu \int \frac{d\phi}{2\pi} \int d\mu' \int d\phi' \int d\mathbf{k}' k'^2 P^{\text{true}}(k', \mu') \\ &\times \sum_{ij, i \neq j}^{N_{\text{ran}}} w_{\text{FKP}}(\mathbf{x}_i) w_{\text{FKP}}(\mathbf{x}_j) e^{i\mathbf{k} \cdot \Delta \mathbf{x}} e^{-i\mathbf{k}' \cdot \Delta \mathbf{x}} \mathcal{L}_\ell(\mu), \end{aligned} \quad (\text{B.1})$$

where $\Delta \mathbf{x} = \mathbf{x}_i - \mathbf{x}_j$. We now expand the power spectrum into multipoles $P(k', \mu') = \sum_L P_L(k') \mathcal{L}_L(\mu')$ where $\mu' = \hat{\mathbf{k}}' \cdot \hat{\mathbf{x}}_h$. We also apply the relation

$$e^{i\mathbf{k} \cdot \mathbf{x}} = \sum_s i^s (2s + 1) j_s(|\mathbf{k}| |\mathbf{x}|) \mathcal{L}_s(\mu), \quad (\text{B.2})$$

as well as the identity

$$\begin{aligned} \frac{2\ell + 1}{2} \int d\mu \int \frac{d\phi}{2\pi} \mathcal{L}_\ell(\hat{\mathbf{k}} \cdot \Delta \hat{\mathbf{x}}) \mathcal{L}_{\ell'}(\hat{\mathbf{k}}' \cdot \hat{\mathbf{x}}_h) \\ = \mathcal{L}_\ell(\hat{\mathbf{x}}_h \cdot \Delta \hat{\mathbf{x}}) \delta_{\ell\ell'}. \end{aligned} \quad (\text{B.3})$$

See Appendix B3 for a proof of this identity. We can now re-write the convolution as

$$\begin{aligned} P_\ell^{\text{conv}}(k) &= 2\pi \int d\mathbf{k}' k'^2 \sum_L P_L^{\text{true}}(k') (-i)^L \\ &\times 2i^\ell (2\ell + 1) \sum_{ij, i \neq j}^{N_{\text{ran}}} w_{\text{FKP}}(\mathbf{x}_i) w_{\text{FKP}}(\mathbf{x}_j) \\ &\times j_\ell(k|\Delta \mathbf{x}|) j_L(k'|\Delta \mathbf{x}|) \mathcal{L}_\ell(\hat{\mathbf{x}}_h \cdot \Delta \hat{\mathbf{x}}) \mathcal{L}_L(\hat{\mathbf{x}}_h \cdot \Delta \hat{\mathbf{x}}). \\ &= 2\pi \int d\mathbf{k}' k'^2 \sum_L P_L^{\text{true}}(k') |W(k, k')|_{\ell L}^2 \end{aligned} \quad (\text{B.4})$$

with the window function defined as

$$\begin{aligned} |W(k, k')|_{\ell L}^2 &= 2i^\ell (-i)^L (2\ell + 1) \sum_{ij, i \neq j}^{N_{\text{ran}}} w_{\text{FKP}}(\mathbf{x}_i) w_{\text{FKP}}(\mathbf{x}_j) \\ &\times j_\ell(k|\Delta \mathbf{x}|) j_L(k'|\Delta \mathbf{x}|) \mathcal{L}_\ell(\hat{\mathbf{x}}_h \cdot \Delta \hat{\mathbf{x}}) \mathcal{L}_L(\hat{\mathbf{x}}_h \cdot \Delta \hat{\mathbf{x}}). \end{aligned} \quad (\text{B.5})$$

This equation does not depend on the vector \mathbf{k} anymore (but only its amplitude k) and hence does not scale with the number of modes N_c .

B2 Integral constraint: derivation of equation (36)

We start with the observed density field (Peacock & Nicholson 1991)

$$\delta'(\mathbf{x}) W(\mathbf{x}) = W(\mathbf{x}) \left[\delta(\mathbf{x}) - \int d\mathbf{x} \delta(\mathbf{x}) W(\mathbf{x}) \right], \quad (\text{B.6})$$

where the second term on the right comes from the assumption that the mean density of the survey is equal to the mean density of the Universe. The density field measured with a galaxy survey has the survey window function $W(\mathbf{x})$ imprinted. In Fourier space this equation becomes

$$\begin{aligned} \int d\mathbf{k}' \delta'(\mathbf{k}') W(\mathbf{k} - \mathbf{k}') &= \int d\mathbf{k}' \delta(\mathbf{k}') W(\mathbf{k} - \mathbf{k}') \\ &- \frac{W(\mathbf{k})}{W(0)} \int d\mathbf{k}' \delta(\mathbf{k}') W(\mathbf{k}'). \end{aligned} \quad (\text{B.7})$$

Taking $\langle \delta' \delta'^* \rangle$ we get equation (29). Focusing on the integral constraint for multipoles, we can write

$$\begin{aligned} P_\ell^{\text{ic}}(k) &= \frac{2\ell + 1}{2} \int d\mu \int \frac{d\phi}{2\pi} \frac{|W(\mathbf{k})|^2}{|W(0)|_0^2} \\ &\times \left[\int d\mathbf{k}' P^{\text{true}}(\mathbf{k}') |W(\mathbf{k}')|^2 \right] \mathcal{L}_\ell(\mu) \\ &= 2\pi \frac{|W(\mathbf{k})|_\ell^2}{|W(0)|_0^2} \int d\mathbf{k}' k'^2 \sum_L P_L^{\text{true}}(k') |W(k')|_{\ell L}^2 \frac{2}{2L + 1} \end{aligned} \quad (\text{B.8})$$

with the window function

$$|W(k)|_\ell^2 = \frac{2\ell + 1}{2} \int d\mu \int \frac{d\phi}{2\pi} W(\mathbf{k}) W^*(\mathbf{k}) \mathcal{L}_\ell(\mu) \quad (\text{B.9})$$

$$\begin{aligned} &= \frac{2\ell + 1}{2} \int d\mu \int \frac{d\phi}{2\pi} \sum_{ij, i \neq j}^{N_{\text{ran}}} w_{\text{FKP}}(\mathbf{x}_i) w_{\text{FKP}}(\mathbf{x}_j) \\ &\times e^{i\mathbf{k} \cdot \mathbf{x}_i} e^{-i\mathbf{k} \cdot \mathbf{x}_j} \mathcal{L}_\ell(\mu) \end{aligned} \quad (\text{B.10})$$

$$\begin{aligned} &= i^\ell (2\ell + 1) \sum_{ij, i \neq j}^{N_{\text{ran}}} w_{\text{FKP}}(\mathbf{x}_i) w_{\text{FKP}}(\mathbf{x}_j) \\ &\times j_\ell(k|\Delta \mathbf{x}|) \mathcal{L}_\ell(\mathbf{x}_h \cdot \Delta \hat{\mathbf{x}}). \end{aligned} \quad (\text{B.11})$$

For this derivation we used equation (B.2) and the identity relation (B.3) in the same way as we did in the last section.

B3 Proof of the identity relation in equation (B.3)

We want to prove

$$\begin{aligned} \frac{2\ell+1}{2} \int d\mu \int \frac{d\phi}{2\pi} \mathcal{L}_\ell(\hat{\mathbf{k}} \cdot \Delta\hat{\mathbf{x}}) \mathcal{L}_{\ell'}(\hat{\mathbf{k}} \cdot \hat{\mathbf{x}}_h) \\ = \mathcal{L}_\ell(\hat{\mathbf{x}}_h \cdot \Delta\hat{\mathbf{x}}) \delta_{\ell\ell'} \end{aligned} \quad (\text{B.12})$$

To do this we are going to use

$$\mathcal{L}_\ell(\hat{\mathbf{k}} \cdot \hat{\mathbf{k}}') = \frac{4\pi}{2\ell+1} \sum_{m=-\ell}^{\ell} Y_{\ell m}(\hat{\mathbf{k}}) Y_{\ell m}^*(\hat{\mathbf{k}}') \quad (\text{B.13})$$

and

$$\int d\mu \int d\phi Y_{\ell m}(\hat{\mathbf{k}}) Y_{\ell' m'}^*(\hat{\mathbf{k}}) = \delta_{\ell\ell'} \delta_{mm'}, \quad (\text{B.14})$$

where the spherical harmonics are given by

$$Y_\ell^m(\hat{\mathbf{k}}) = (-1)^m \sqrt{\frac{(2\ell+1)(\ell-m)!}{4\pi(\ell+m)!}} \mathcal{L}_\ell^m(\mu) e^{im\phi}, \quad (\text{B.15})$$

with $\hat{\mathbf{k}} = (\theta, \phi)$ and $\mu = \cos(\theta)$. We start with the left-hand side of equation (B.12):

$$\begin{aligned} \frac{2\ell+1}{2} \int d\mu \int \frac{d\phi}{2\pi} \mathcal{L}_\ell(\hat{\mathbf{k}} \cdot \Delta\hat{\mathbf{x}}) \mathcal{L}_{\ell'}(\hat{\mathbf{k}} \cdot \hat{\mathbf{x}}_h) \\ = \frac{2\ell+1}{2} \int d\mu \int \frac{d\phi}{2\pi} \frac{4\pi}{2\ell+1} \sum_{m=-\ell}^{\ell} Y_{\ell m}(\hat{\mathbf{k}}) Y_{\ell m}^*(\Delta\hat{\mathbf{x}}) \end{aligned} \quad (\text{B.16})$$

$$\times \frac{4\pi}{2\ell'+1} \sum_{m'=-\ell'}^{\ell'} Y_{\ell' m'}^*(\hat{\mathbf{k}}) Y_{\ell' m'}(\hat{\mathbf{x}}_h) \quad (\text{B.17})$$

$$= \frac{2\ell+1}{4\pi} \left(\frac{4\pi}{2\ell+1} \right)^2 \sum_{m=-\ell}^{\ell} Y_{\ell m}^*(\Delta\hat{\mathbf{x}}) Y_{\ell m}(\hat{\mathbf{x}}_h) \delta_{\ell\ell'} \quad (\text{B.18})$$

$$= \mathcal{L}_\ell(\hat{\mathbf{x}}_h \cdot \Delta\hat{\mathbf{x}}) \delta_{\ell\ell'} \quad (\text{B.19})$$

APPENDIX C: MULTIVARIATE GAUSSIAN WITH THE SOUND HORIZON FROM EISENSTEIN & HU (1998)

Here we provide the multivariate Gaussian likelihood using the sound horizon calculated from the approximate equation in Eisenstein & Hu (1998) while in Section 8.3 we used the sound horizon calculated with CAMB. The ratio of the two calculations is roughly 1.026 and when treated consistently both methods should lead to the same conclusions (see Mehta et al. 2011 for details). For the fitting range $k = 0.01\text{--}0.20 h \text{Mpc}^{-1}$ we have

$$V_{k_{\text{max}}=0.20}^{\text{data}} = \begin{pmatrix} D_V(z_{\text{eff}})/r_s^{\text{EH}}(z_d) \\ F(z_{\text{eff}}) \\ f(z_{\text{eff}})\sigma_8(z_{\text{eff}}) \end{pmatrix} = \begin{pmatrix} 13.53 \\ 0.683 \\ 0.422 \end{pmatrix} \quad (\text{C.1})$$

and the symmetric covariance matrix is given by

$$10^3 C_{k_{\text{max}}=0.20} = \begin{pmatrix} 34.576 & -2.0110 & -1.7926 \\ & 1.0776 & 1.1757 \\ & & 1.8475 + 0.196 \end{pmatrix} \quad (\text{C.2})$$

leading to

$$C_{k_{\text{max}}=0.20}^{-1} = \begin{pmatrix} 32.668 & 79.761 & -17.231 \\ & 2686.8 & -1475.8 \\ & & 1323.3 \end{pmatrix}. \quad (\text{C.3})$$

For $f\sigma_8$ we included the systematic error of 3.1 per cent (see Section 7), where we assumed uncorrelated systematic errors. The sound horizon scale derived with the approximate equation in Eisenstein & Hu (1998) is $r_s(z_d) = 151.28 \text{Mpc}$.

The maximum likelihood values for the fitting range $k = 0.01\text{--}0.15 h \text{Mpc}^{-1}$ are

$$V_{k_{\text{max}}=0.15}^{\text{data}} = \begin{pmatrix} D_V(z_{\text{eff}})/r_s^{\text{EH}}(z_d) \\ F(z_{\text{eff}}) \\ f(z_{\text{eff}})\sigma_8(z_{\text{eff}}) \end{pmatrix} = \begin{pmatrix} 13.48 \\ 0.684 \\ 0.420 \end{pmatrix} \quad (\text{C.4})$$

and the symmetric covariance matrix is given by

$$10^3 C_{k_{\text{max}}=0.15} = \begin{pmatrix} 82.202 & -5.7200 & -3.0557 \\ & 2.2844 & 1.9768 \\ & & 2.9510 \end{pmatrix} \quad (\text{C.5})$$

leading to

$$C_{k_{\text{max}}=0.15}^{-1} = \begin{pmatrix} 15.388 & 58.870 & -23.503 \\ & 1266.8 & -787.65 \\ & & 842.17 \end{pmatrix}, \quad (\text{C.6})$$

where no systematic error is included.

¹Lawrence Berkeley National Lab, 1 Cyclotron Rd, Berkeley, CA 94720, USA

²Kavli Institute for the Physics and Mathematics of the Universe (WPI), Todai Institutes for Advanced Study, The University of Tokyo, Chiba 277-8582, Japan

³Department of Astronomy, University of California, Berkeley, CA 94720, USA

⁴Department of Physics, University of California, Berkeley, CA 94720, USA

⁵Berkeley Center for Cosmological Physics, LBL and Department of Physics, University of California, Berkeley, CA 94720, USA

⁶Department of Physics, Center for Cosmology and Astroparticle Physics, The Ohio State University, OH 43210, USA

⁷Apache Point Observatory, PO Box 59, Sunspot, NM 88349-0059, USA

⁸Department of Physics and Astronomy, University of Utah, Salt Lake City, UT 84112, USA

⁹Harvard-Smithsonian Center for Astrophysics, 60 Garden St., Cambridge, MA 02138, USA

¹⁰Department of Physics, Carnegie Mellon University, 5000 Forbes Avenue, Pittsburgh, PA 15213, USA

¹¹McWilliams Center for Cosmology, Carnegie Mellon University, 5000 Forbes Avenue, Pittsburgh, PA 15213, USA

¹²Max-Planck-Institut für Extraterrestrische Physik, Giessenbachstrasse, D-85748 Garching, Germany

¹³Institute of Cosmology & Gravitation, Dennis Sciama Building, University of Portsmouth, Portsmouth PO1 3FX, UK

¹⁴Department of Physics, Drexel University, 3141 Chestnut Street, Philadelphia, PA 19104, USA

¹⁵Center for Cosmology and Particle Physics, New York University, New York, NY 10003, USA